This is a preprint, the final version is subject to change, of the American Mineralogist (MSA)
Cite as Authors (Year) Title. American Mineralogist, in press.
DOI: https://doi.org/10.2138/am-2020-7341

Revision including Associate Editor's and reviewer's comments (7/12/2019)

New insights into the nature of glauconite

ADRIÁN LÓPEZ-QUIRÓS[1*] ANTONIO SÁNCHEZ-NAVAS[1, 2], FERNANDO NIETO[1, 2], CARLOTA ESCUTIA[1]

[1]Instituto Andaluz de Ciencias de la Tierra, CSIC-University of Granada, 18100 Armilla, Granada, Spain. [2]Department of Mineralogy and Petrology, University of Granada, 18071 Granada, Spain. *E-mail: *alquiros@iact.ugr-csic.es*

ABSTRACT

Glauconite must be assessed as mica-rich mica-smectite R3 interstratified mineral, with the pure end-member mica having also intrinsic K-deficient chemical characteristic (K^+ ~ 0.8 a.p.f.u.). This assertion is in accordance with our XRD and HRTEM studies and chemical analyses (EPMA) of mature glauconites in Cenozoic Antarctic sediments which indicate that: (1) It consists of a glauconite-smectite (R3 ordered) mixed-layer silicate, composed mainly of mica-type layers (> 90%), but displaying slightly different proportions of Fe(III)-smectite layers (< 10%). (2) More mature glaucony grains are characterized by major K^+ and $^{VI}Fe^{2+}$ (mica layers) and minor $^{VI}Fe^{3+}$ (smectite layers) content in the interstratified glauconite-smectite. (3) Potassium is stabilized at the interlayer site by the octahedrally coordinated Fe^{2+}. (4) Microtexture of the glauconite crystals are comparable with those of other micas and illite minerals, with straight, defect-free lattice fringes of ~10Å spacings glauconite packets characteristic of mica with minor interstratified poorly crystalline smectite layers. In addition, our new findings give insights into the glauconitization process and at the same time investigate

the potassium-deficient character of the dioctahedral mica '*glauconite'*. These findings show that glauconite crystallize by a layer-growth mechanism at expense of a poorly crystalline smectite precursor, and that smectite-to-glauconite transformations are accompanied by a gradually higher octahedral charge deficiency (Fe^{2+}/Fe^{3+}) stabilized by K^+ uptake into the interlayer sheet.

Keywords: Glaucony, Glauconite, Interstratified Glauconite-Smectite, HRTEM, XRD.

INTRODUCTION

'Glauconite' sensu strictu is a dioctahedral, K- and Fe-rich 2:1 interlayer-deficient mica. According to the AIPEA (*Association Internationale Pour I'Étude des Argiles*; Bailey, 1980), the mineral glauconite is defined by: (1) $^{IV}Al^{3+}$ (or $^{IV}Fe^{3+}$) > 0.2 atoms per formula unit (a.p.f.u.) based on $O_{10}(OH)_2$; (2) $^{VI}R^{3+}$ > 1.2 a.p.f.u., with $^{VI}Mg^{2+}$ > $^{VI}Fe^{2+}$ and $^{VI}Fe^{3+}$ > $^{VI}Al^{3+}$; (3) the basal reflection *d*001 located between 14Å and 10Å, *d*020 at 4.53Å, *d*003 at 3.33Å, and *d*060 at 1.51Å; and (4) potassium occupying mostly the interlayer sheet (K^+ > 0.6 a.p.f.u.). The IMA (*International Mineralogical Association*; Rieder et al., 1999) described glauconite as a Fe-rich phyllosilicate (dioctahedral interlayer-deficient mica) mineral with a green color and representative formula: $K_{0.8}R^{3+}_{1.33}R^{2+}_{0.67}Al_{0.13}Si_{3.87}O_{10}(OH)_2$, in which $^{VI}R^{2+}/(^{VI}R^{2+}+^{VI}R^{3+}) \geq 0.15$ and $^{VI}Al/(^{VI}Al+^{VI}Fe^{3+}) \leq 0.5$. The term *'glauconitic'* (suggested nomenclature in Odin and Fullagar, 1988) is used for the minerals of the *'glaucony facies'* (Odin and Létolle, 1980), which cover a complete genetically related mineral series from Fe-rich smectite to Fe-rich illite, i.e. the glauconitic mica, which is the end-member type of the glaucony facies.

Although the precise process and timing of glauconite genesis is still under debate, diverse mechanisms have been involved to interpret the formation of glauconite (e.g. Galliher, 1935; Burst, 1958; Hower 1961; Ehlmann et al., 1963; Ojakangas and Keller, 1964; Harder, 1980; Odin and Matter, 1981; Odin and Fullagar, 1988). Odin and Matter (1981) and Odin and Fullagar (1988) summarized the state of knowledge on the glauconitization process, and proposed to date the widely accepted *'precipitation-dissolution-recrystallization theory'*. This theory includes a two-stage glauconitization model where mature glauconite formation involves two major phases: (1) the formation of a K-poor, Fe-rich glauconitic smectite (the Fe(III)-rich smectite precursor; Fig. 1), and (2) a gradual enrichment with K^+ to form a K-rich glauconitic mica (the Fe(III)-smectite-to-glauconite reaction; Fig. 1). Therefore, the glauconitization process is a low-temperature diagenetic phenomenon that can be classified based on the K_2O wt% (Odin and Matter, 1981; Odin and Fullagar, 1988) (Fig. 1). The degree of evolution of the glauconitization process depends on the residence time of glaucony grains in confined sub-oxic, partially reduced microenvironments at or near the sediment-water interface, and hence the sedimentation rate is a key factor (e.g. Amorosi, 1995; 2012).

The differences between glauconite and other green-clay minerals, such as Fe-illite or celadonite, are very subtle and hence, the nature of glauconite is still challenging. Odin and Matter (1981) discussed a compositional gap between illitic minerals ($Fe_2O_3 <$ 10%) and glauconitic minerals ($Fe_2O_3 >$15%). Later researchers, nevertheless, reported a compositional continuum between these two minerals (e.g. Ireland et al., 1983; Deb and Fukuoka, 1998). Celadonite has also been excluded as a feasible glauconite parent mineral material by its higher octahedral layer charge, and higher Si content (Duplay and Buatier, 1990; Huggett, 2005).

Recent studies on green-clay (glaucony) authigenic minerals (e.g. Charpentier et al., 2011; Gaudin et al., 2005; Baldermann et al., 2013) highlights the bacterially-mediated neoformation of Fe-rich smectitic clays as the most plausible precursor mineral phase of the glauconitization process, which is in agreement with the theory of Odin and Matter (1981). In this respect, Fe-rich smectite formation is reported in the literature related to glauconitization process (e.g. Harder, 1980; Amouric and Parron, 1985; Martín-Algarra and Sánchez-Navas, 1995; Jiménez-Millán et al., 1998; Kloprogge et al., 1999; Gaudin et al., 2005; Baldermann et al., 2012, 2013).

The internal fabric of glauconite has been previously studied by HRTEM in order to shed light on the mechanism involved in the glauconitization process. Amouric and Parron (1985) described the occurrence of smectite-rich zones sandwiching glauconite packets, with a sharp interface between them, but according to their HRTEM study no interlayering of glauconite and smectite was observed. Buatier et al. (1989) reported the presence of lath-shaped glauconite crystallites that appeared to be sandwiched together with Fe-smectite-like layers, forming an irregular 'interstratified' stacking sequence. They found that glauconite crystallites are commonly oriented parallel to the smectite layers, but also reported a structural discontinuity (i.e. absence of lattice fringes) between the glauconitic and smectitic layers. Jiménez-Millán et al. (1998) reported glauconite crystallites and also poorly crystalline areas with smectitic composition that could represent the remains of a glauconitic precursor. These authors did not observe a textural transitional relationship between smectite and glauconite. More recently, particles having variable *d*(001) spacing and an intermediate composition between glauconite and smectite were referred to as mixed-layered glauconite-smectite phases by Baldermann et al. (2013, 2015).

The purpose of the present research is to explore the K-deficient character of the dioctahedral mica 'glauconite', to determine its mineralogical significance and its relation to the presence of variable smectite interstratifications during glaucony maturation.

GEOLOGICAL SETTING AND LITHOSTRATIGRAPHY

Samples of glaucony-bearing facies were taken from the late Eocene and Oligocene-Miocene transition sediments recovered by the Ocean Drilling Program (ODP), Leg 113 at Site 696 (Cores 57-56R and 51-52R, respectively), which are located in the South Orkney Microcontinent (SOM) in the northwestern Weddell Sea (Antarctica) (Fig. 2A and B).

The SOM is the largest (~250 x 350 km) continental fragment of the South Scotia Ridge (SSR) between the Scotia and Antarctic plates (Fig. 2A), and is a remnant of the original link connecting the Antarctic Peninsula and South America. The SOM was disconnected from the Antarctic Peninsula along an E-W margin, probably during the Eocene and early Oligocene (40–30 Ma; King and Barker, 1988). The SOM then continued to drift and rotate eastward until it reached its current position with respect to the Antarctic Peninsula during the early Miocene (King and Barker, 1988; Coren et al., 1999). The southeast and southwest SOM passive margins are connected to the proto-oceanic Powell and the oceanic Jane basins respectively (Fig. 2A), formed after the rifting between the Antarctic Peninsula and the SOM.

At ODP Site 696, hemipelagic (from the seafloor to about 214 mbsf), pelagic (from about 214 to 530 mbsf), and terrigenous to authigenic (from 530 mbsf to the base of the hole) sediments deposited between the Late Eocene and the Quaternary (Barker et al.,

1988; Wei and Wise, 1990; Gersonde and Burckle, 1990; Fig. 2B). The late Eocene-lower middle Miocene terrigenous *Unit VII* (530 mbsf to base of hole at 646 mbsf) is distributed in four subunits (*VIID*, *VIIC*, *VIIB* and *VIIA*; Fig. 2B) (Barker et al., 1988). This study focuses on sediments recovered at subunits *VIIC* and *VIIA*. *Subunit VIID* (early late Eocene, 645.6 to 606.9 mbsf) is depicted by sandy mudstone and minor clayey mudstone facies. The latest Eocene sediments of *Subunit VIIC* (569.7 to 606.9 mbsf) are characterized by high amounts of glaucony grains interpreted as autochthonous (evolved; K^+ >0.66 a.p.f.u.) smectite-poor interstratified ~10Å glauconite-smectite (López-Quirós et al., 2019) (Fig. 2C, F, I). López-Quirós et al. (2019) also reported the occurrence of scarcely altered to nontronite reworked glaucony within the condensed glauconitic section deposited at the SOM shelf during the latest Eocene. These altered glaucony grains were not taken into account for the present work. Major lithologies within *Subunit VIIB* (early Oligocene, 548.9 to 579.4 mbsf) include claystone and clayey mudstone facies, with minor silty mudstone occurrences at the base of this subunit; both lithologies contain minor amounts of glaucony grains. The sediments of *Subunit VIIA* (Oligocene-Miocene, 529.8 to 548.9 mbsf; Barker et al., 1988) are characterized by rhythmically interbedded sandy mudstone with glauconite-bearing sandstone beds. A significantly different picture arises from glaucony grains deposited at *Subunit VIIA*. Allochthonous (detrital) glaucony grains (Fig. 2D, E, G, H) are interpreted here to have been reworked from condensed green sections belonging to Eocene sequences in the vicinity of the SOM shelf, deposited under abundant bottom currents and possibly slumping action. Some of these reworked glaucony grains exhibits altered zones, forming rims around grains and along cracks (e.g. Fig. 2E). These grains were likewise not taken into account for this work, since the post-depositional reversal of the glauconitization process (i.e. smectitization) partially transformed the glauconite

mineral. Therefore, this work only uses unaltered glaucony grains. The stratigraphic age control was base on calcareous nannofossils and diatoms (see Barker et al 1988; Wei and Wise, 1990; Gersonde and Burckle, 1990), recently updated through dinocysts stratigraphy by Houben et al. (2013, 2019) (Fig. 2B).

ANALYTICAL METHODS

The distribution of glaucony-bearing facies within the transgressive condensed sequence deposited between the late Eocene-lower middle Miocene ODP Hole 696B, is related to distinct environments of mineral formation controlled by paleogeography (e.g. López-Quirós et al., 2019). Samples of these glaucony-bearing sediments for this study were obtained from sediment cores 57-56R (~588.5 to 578 mbsf) and 51-52R (~540 to 531 mbsf) (Fig. 2). Glaucony grains were extracted (disaggregated and washed) from the whole rocks on a 125 and 250µm screen. These fractions were later separated magnetically by an electromagnetic universal UMC-1 separator. Purified glaucony particles were further separated from diagenetic complex growths and aggregates along with other sediment grains under binocular microscope. Eight thin sections, about 30µm thick, were prepared by epoxy impregnation in order to fill the pores and consolidate some poorly lithified glauconitic packstone samples from cores 57-56R.

The X-ray-diffraction (XRD) data were obtained from powder glaucony grain concentrates (reduced in size with an agate mortar) and oriented aggregates of the <2µm fraction treated with ethylene glycol, with a PANalytical X'Pert Pro diffractometer (CuKα radiation, 45 kV, 40 mA) equipped with an X'Celerator solid-state linear detector (Department of Mineralogy and Petrology, University of Granada). Data were collected for 10 sec in 0.008° 2θ steps. Decomposition routines included in the

HighScore software were applied in order to depict the superposition of glauconite and smectite mixed-layers on the *d*-001 peaks at 10Å for glauconite. Peaks were fitted through a Voigt function (mixed Gaussian and Lorentzian). Various combinations of peaks were proven until we acquired the lowest residuum. Intensity, half-height width and peak position were approximated by the least-squares method until they optimally retraced the peak course of the original profile.

Electron probe microanalysis (EPMA) of the main glaucony-forming elements was carried out with a CAMEBAX SX-100 automated electron microprobe (CIC, University of Granada) in the wavelength dispersive mode under the following conditions: acceleration voltage 15kV, probe current 15nA, electron beam diameter 5µm. Calibration standards were mineral albite (Na), diopside (Si), sanidine (K), wollastonite (Ca), rhodonite (Mn), TiO_2 (Ti), CaF_2 (F), and Fe_2O_3 (Fe) and synthetic periclase (Mg), and Al_2O_3 (Al).

High-resolution transmission electron microscopy (HRTEM) photomicrographs were conducted with a Titan instrument with XFEG emission gun, spherical aberration corrector and HAADF detector, operated at 300kV accelerating voltage. The point-to-point resolution of this apparatus is 0.8Å in the HRTEM mode and 2Å in the scanning transmission electron microscopy (STEM) mode (CIC, University of Granada). Copper rings were attached to selected glaucony zones of previously studied thin-sections from cores 57R and 52R. These selected zones were separated later through moderate heating. Glaucony samples were further thinned with a Fischione Model 1050 ion mill operating with an accelerating voltage of 4 kV and ±10°, until the first hole and ±7° during 20 min for final cleaning and finally carbon coated. The same powder used for the XRD analyses was also used for quantitative chemical analyses in STEM mode. Powdered glaucony concentrates were dispersed in ethanol solution, sonicated, and deposited on a

thin carbon film coated upon several Cu grids. Quantitative chemical analyses were acquired using the SuperX detector of the Titan. Mineral standards were used to obtain K-factors according to the method proposed by Cliff and Lorimer (1975). Furthermore, selected-area electron diffraction (SAED) patterns were acquired of glauconite crystals with the same instrument.

XRD, HRTEM AND COMPOSITIONAL DATA

Powder XRD air-dried diagrams of the purified glaucony concentrates from both, the late Eocene autochthonous grains (Fig. 3A, B) and Oligocene-Miocene allochthonous grains (Fig. 3C, D), revealed d_{001} reflections of glauconite at ~10Å. After deconvolution of ethylene glycol treated samples, peak at ~10Å (d_{001G} in Fig. 3 A, C) is formed by two peaks at 9.8 Å and ~11Å (Fig. 3B, D). The fact that intensity of the d_{001G} high-order basal peak is decreased slightly when samples are ethylene-glycol-saturated, denotes the presence of a small number of expandable layers. A weak d_{002} reflection at ~5Å, and a strong d_{003} reflection at ~3.3Å were also observed (e.g. Fig. 3A). The observed weak and broad d_{001S} peaks between 12-14Å, which shifted between 17-19Å after glycolation (see Fig. 3B, D), indicated the presence of smectite or an illite-smectite (R0 disordered) mixed-layer, constituted mainly by smectite layers. This data are in agreement with previously reported detrital glaucony replacements by nontronite ('smectitization' or reversal of the glauconitization process) at ODP Hole 696B (Fig. 2E and López-Quirós et al., 2019). Significant plagioclase content in the Oligocene-Miocene glaucony concentrates is also revealed by XRD (Fig. 3C). Abundant plagioclase (anorthite) crystals in the glaucony-bearing rock matrix were depicted here. Thus, plagioclase peaks identified at the glaucony concentrated XRD diagrams (e.g. Fig. 3C), are

224 probably due to non-complete glaucony grain purification during the Oligocene-
225 Miocene sample preparation and/or original inclusion of plagioclase crystals into the
226 pellets.

227 According to the peak spacing and its ethylene-glycol-solvated behavior, XRD
228 diagrams may be interpreted as a glauconite-smectite (R3 ordered) mixed-layer silicate,
229 composed mainly of mica-type layers (> 90%), but displaying slightly different
230 proportions of interstratified smectite layers (< 10%) (see for comparison Moore and
231 Reynolds, 1997; Fig. 4).

232 HRTEM images of the studied late Eocene autochthonous and Oligocene-Miocene
233 allochthonous grains show well-defined ~10Å lattice fringes of glauconite crystals (Fig.
234 5) and 9.90Å d_{001}-spacing in SAED patterns (Fig. 5A, D). Lattice images display the
235 typical lamellar arrangement of glauconite packets with a d = 10Å spacing,
236 characteristic of both mica and contracted-smectite layers (2:1 silicate layer; e.g. Fig.
237 5B-F). SAED patterns likewise reflect the subparallel stacking of glauconite crystal
238 packets (Fig. 5A, D). Representative chemical formulae obtained from complementary
239 AEM analyses of late Eocene autochthonous grains are included in Table 1. The
240 formula derived from AEM results of the overall interstratified glauconite/smectite
241 phase of late Eocene crystals, revealed slightly lower K^+ content (~0.6 a.p.f.u) than
242 observed by EPMA (see below). The differences in K^+ content and total interlayer
243 occupancy could be mainly due to potassium volatilization during the AEM-EDX study
244 (Van der Pluijm et al, 1988).

245 EPMA data of the studied glaucony samples are likewise in agreement with the XRD
246 and with HRTEM results. Thus, the amounts of interlayer K^+ in the normalized formula
247 to $O_{10}(OH)_2$ after EPMA results, is between 0.62 and 0.75 (a.p.f.u.) for late Eocene
248 autochthonous glaucony, and between 0.61 and 0.71 (a.p.f.u.) for Oligocene-Miocene

allochtonous glaucony grains (Tables 2, 3 and Fig. 6). The compositional range of the octahedral sheet in both, the late Eocene and Oligocene-Miocene glaucony grains, is depicted by high Fe ($Fe^{2+} + Fe^{3+}$), low to moderate Mg, and low Al contents (Tables 2, 3 and Fig. 6).

DISCUSSION

The glauconitization process: smectite-to-glauconite transformations

Although many mineralogical models for the glauconitization have been presented over last decades (e.g. Galliher, 1935; Burst, 1958; Hower 1961; Ehlmann et al., 1963; Ojakangas and Keller, 1964; Harder, 1980; Odin and Matter, 1981; Odin and Fullagar, 1988), the accurate process of glauconite genesis is still under debate.

The first stage in the glauconitization process is characterized by the formation of a glauconitic precursor, but the nature of this precursor has remained obscure. Odin and Fullagar (1988) suggested that during this early-authigenic stage, crystals growth from a smectite precursor is shaped in the substrate pores by using cations from seawaters and interstitial waters (Fig. 1). Later researchers, nevertheless, proposed other phyllosilicate minerals as a plausible precursor of the glauconitization process, such as glauconitic clay (e.g. Stille and Clauer, 1994), or a kaolinite-smectite bearing substratum (e.g. Galan et al., 1995). In the last years, however, the most widely accepted conceptual reaction model proposed for the glauconitization comprise the very early diagenetic precipitation of a Fe(III)-smectite precursor within a few thousand years, which is promoted by microbial activity working as a catalyzer along with cation supply from porewaters by aqueous ion diffusion (Wiewióra et al., 2001; Gaudin et al., 2005;

Charpentier et al., 2011; Baldermann et al., 2013) (Fig. 1). For example, Reolid and Abad (2014) pointed out the role of chemoorganotrophic microbes, as well as the passive mineralization of the extracellular polymeric substances in the origin and growth of glauconitic laminated crusts under low-temperature hydrothermal conditions. Microbial activity has also been reported in glaucony-bearing deposits formed in different geological palaeogeographic settings (Sánchez-Navas et al., 1988; Martín-Algarra and Sánchez-Navas, 2000; Zanin et al., 2004; Eder et al., 2007; Sánchez-Navas et al., 2008). In this respect, Fe(III)-smectite precipitation from a non-crystalline previous phase (i.e. an amorphous gel-like substance) was proposed by Harder (1980), Jiménez-Millán et al. (1998), Kloprogge et al. (1999), Gaudin et al. (2005), and Baldermann et al. (2012; 2013). López-Quirós et al. (2019) comparably, observed textural remains supporting a microbial origin for the precipitation of early glauconitic structures from a likely bacteria-produced gel stage during the late Eocene glauconitization event at ODP Hole 696B. Based on HRTEM and AEM analyses, other investigations also have supported the proposed early glauconitization process depicted by a precursor non-crystalline phase from which the smectite crystallizes (e.g. Amouric and Parron, 1985; Amouric, 1990; Martín-Algarra and Sánchez-Navas, 1995; Jiménez-Millán et al., 1998). Likewise, Jiménez-Millán and Castro (2008) pointed out about a Si-Al-rich poorly crystalline substance filling K-feldspar micropores of alternating packets of glauconite and berthierine layers. Amouric and Parron (1985) and Amouric (1990), likewise determined by XRD the formation of a *d*001 ~ 12.5Å smectite (of Fe-beidellite or Fe-montmorillonite type) phase, related to the development of a precursor gel in the earliest glauconitization stage.

Our HRTEM data revealed the occurrence of individual smectite layers between the glauconite packets (i.e. the smectite precursor from which glauconite was crystallized)

(Fig. 5). Although we have not identified the presence of a precursor gel-like phase, the occurrence of these smectite areas (Fig. 5B, E), suggests that their origin might be concomitant with the existence of a poorly crystalline precursor material. This is supported by the accepted mineralized spheroidal and tubular capsules interpreted as bacterial remains in early glauconitic structures in the late Eocene sediments from Hole 696B by López-Quirós et al. (2019). Therefore, our XRD, EPMA and HRTEM interpretations point out to the smectite-to-glauconite transformation to have been formed by a layer-growth mechanism at the expense of a previous smectite precursor. The layer-growth mechanism observed for glauconite explains the typical lamellar microstructure of the mineral as seen by HRTEM and SEM (Fig. 2F, G, I). The gel-like phase during the evolutive process of glauconitization hitherto considered by Harder (1980), Jiménez-Millán et al. (1998), Kloprogge et al. (1999), Gaudin et al. (2005), Baldermann et al. (2012, 2013), among many others, was not recorded by our HRTEM study.

The second stage in the glauconitization process is characterized by the Fe(III)-smectite to glauconite reaction at the very shallow, burial diagenesis (see Fig. 1). Burial to more than a few decimeters halts the glauconitization (Hugget, 2005). Gaudin et al. (2005) discussed that the neoformed Fe(III)-smectite precursor is thermodynamically unstable during early diagenesis and transforms rapidly into glauconite crystals through the formation of interstratified glauconite-smectite. In addition, Meunier and El Albani (2007) and Baldermann et al. (2015) determined that the (bio)availability of Fe^{2+} and K^{+} ions may become as the rate-limiting factor for the green-clay (glaucony) authigenesis. Throughout this maturation stage, glauconite crystal layers are well-known to grow at elevated contents of interlayer K^{+} and structural Fe(II + III) (e.g. Baldermann et al., 2015; 2017); a characteristic corroborated in the present work (Fig. 6C). The

compositional (EPMA) and HRTEM characteristics of the studied glaucony grains are in agreement with this overall substitution of Fe^{3+} for Fe^{2+} and an increase in K^+ during this second (mature) glauconitization stage. The high K^+ contents in the interlayer sites (Tables 2 and 3; Fig. 6), and the abundance of glauconite crystal layers having ~10Å spacings (Fig. 5) suggest a good (evolved *sensu* Odin and Fullagar, 1988) degree of maturation and equilibrium with seawaters. From a mineral-chemical point of view, the reduction of trivalent to bivalent iron (Fe^{3+} to Fe^{2+}) in the octahedral sheet of interstratified glauconite-smectite minerals result in a gradually higher octahedral charge deficiency, stabilized by increased K^+ uptake into the interlayer sheet, as our EPMA data show (Tables 2 and 3; Fig. 6). Smectite-to-glauconite transformations are therefore not only monitored by a K^+ increase at the interlayer sheet, as normally accepted, but also by the increase in Fe^{2+}/Fe^{3+}. Sanchez-Navas et al. (2008) also determined a light absorption produced by the enrichment in octahedrally coordinated Fe^{2+} relative to the total ^{VI}Fe, linked to a progressive reduction in the Fe(III)-smectite content interleaved with glauconite (see also Fig. 4C in López-Quirós et al., 2019). These assumptions lead us to suggest that glauconite could be, thus, neoformed from a Fe(III)-smectite precursor through decomposition-crystallization processes as those proposed by Amouric and Parron (1985) and Amouric (1990).

New insight into the nature of glauconite and glaucony

Glauconite is distinguished from celadonite by its higher octahedral charge as well as higher levels of the substitution of ^{IV}Al for silicon in the tetrahedral site of the mica-based structure (Duplay and Buatier, 1990). In other words, celadonite has higher silica content than glauconite. In addition, celadonite has a higher K^+ (a.p.f.u.) content or

interlayer charge imbalance in the 2:1 structural layer than glauconite (Rieder et al., 1999). Therefore, celadonite has a higher mica charge imbalance in the 2:1 structural layer than glauconite. Calculated octahedral (OC), tetrahedral (TC) and interlayer (IC) charges, and octahedral substitution based on structural formulae are plotted in the charge-distribution diagram given by Köster (1982) in Fig. 7A, with the end-members (1) celadonite, (2) muscovite, and (3) pyrophyllite. Fig. 7A clearly shows that glaucony EPMA results from ODP Hole 696B plot within the glauconite domain.

Glauconite *sensu strictu* displays a mica-type structure, which is compositionally close to the celadonite end-member (Köster, 1982; Fig. 7A). The amount of interlayer K^+ content measured by EPMA ranges between 0.61 and 0.75 a.p.f.u. Slight potassium differences in the K^+ content between interstratified glauconite-smectite, from both stratigraphic levels, have been observed (Fig. 6C, D). Most of these results fit well with its classification as interlayer-cation-deficient mica according to the AIPEA and IMA (Bailey, 1980; Rieder et al., 1999). Moreover, Meunier and El Albani (2007) took into account the interlayer charge to distinguish compositional fields of glaucony and other Fe-bearing clay phases. According to these authors, the compositional domain composed by Fe-Al smectite, glaucony, Fe-illite, Fe-montmorillonite and nontronite, can be distinguished on the basis of $M^+ \cdot (Si/4)^{-1}$ *vs.* $^{VI}Fe\ (II + III)/\Sigma^{VI}$cations cross-plot; where interlayer charge (M^+) = Na+K+2Ca. Nevertheless, the definition of 'glauconitic minerals' proposed by the AIPEA (Bailey, 1980) includes a broad compositional range in glaucony compared to the definition suggested by Meunier and El Albani (2007). Many of our glaucony data do not plot in the glaucony field of Meunier and El Albani (2007) (Fig. 7B), although they satisfy the definition of glauconitic minerals provided by the AIPEA. Furthermore, the octahedral Fe-Al-Mg contents (see Tables 2 and 3), are within the range of typical contents for these elements in glauconite (e.g. Chamley,

1989; Velde, 1992). Total iron measured by EPMA ranges between 1.35 and 1.7 a.p.f.u., with major content in the pristine late Eocene samples (Fig. 6C), which also have major Fe^{2+} content (Fig. 6D, E). The positive correlation between K^+ and $^{VI}Fe^{2+}$ indicates that potassium is stabilized at the interlayer site by the octahedrally coordinated Fe^{2+} (Fig. 6D).

The glauconitization state is given by the positive correlation between the percentage of glauconite layers of the interstratified glauconite-smectite mixed-layer and the interlayer K^+ (a.p.f.u.) content (e.g. Manghnani and Hower, 1964; McRae and Lambert, 1968; Baldermann et al., 2013; Fig. 8). Considering the average interlayer K^+ contents of both, late Eocene (0.68 a.p.f.u.) and Oligocene-Miocene (0.65 a.p.f.u.) stratigraphic sections (see Fig. 2B), EPMA results confirm a mature, glauconite-rich interstratified glauconite-smectite. This is in agreement with powder XRD diagrams, which indicate an interstratified R3-ordered glauconite-smectite clay with more than 90% of mica-type layers (Figs. 4 and 8A, B). Our results also reveal that more mature glauconite are characterized by major K^+ and Fe^{2+} (i.e. mica layers) and minor Fe^{3+} (i.e. smectite layers) content in the interstratified glauconite-smectite.

Our HRTEM images of glauconite crystals are comparable with those of other micas and illite minerals (e.g. Bauluz, 2013). They are widely recognized by their straight, defect-free lattice fringes with constant ~10Å spacings (Fig. 5). The thickness and relative orientation of the crystallite packets may fluctuate according to their genesis. To our knowledge, the interstratified smectite-glauconite phase has not been described in depth by HRTEM up to now, probably due to the challenge of differentiating the collapsed 10Å smectite and glauconite layers. Lattice fringes of glauconite crystals (Fig. 5), characterized by means of their basal reflection planes (*d*001 at 9.9Å; Fig. 5A, D) are mostly located at the central position inside the spindle-

like arrangement of layered crystallite packets. Nevertheless, our lattice images (Fig. 5B-F) also show that the glauconite packets, formed by 9-11 individual layers of mica are systematically interrupted by smectitic layers, showing lighter contrast in the images than those corresponding to mica layers. Such interpretation is supported by image simulation (Guthrie and Veblen, 1989, 1990; Veblen et al, 1990) and is coherent with XRD identification (Figs. 3 and 4). Sometimes the smectitic areas are opened by the irradiation effect of electrons (e.g. Fig. 5E), which allows the identification of the lattice fringes corresponding to opened layers as smectitic (Nieto et al, 1996).

Therefore, the representative lattice images of glauconite included in Fig. 5 can be interpreted as I > 3 mica/smectite mixed-layers in the sense of Bauluz et al. (2000), which would be the major component of a R3 mica/smectite mixed-layers, as determined by XRD (Figs. 3 and 4). The K content determined by EMPA (Tables 2, 3 and Fig. 6) or derived from complementary AEM results (Table 1) is also compatible with a glauconite/smectite mixed-layer having more than 90% of glauconitic layers. This allows us to calculate the percentage of glauconite from the interlayer K^+ content (Fig. 8C).

The studied glauconites of the SOM sequences may be considered representative of mature glauconites as described by the IMA and AIPEA nomenclature committees (Bailey, 1980; Rieder et al., 1999). Based on our results, they show K^+ (a.p.f.u.) content coherent with the maximum described in the literature (Fig. 8). However, according with their detailed XRD and HRTEM analysis they are not micas *sensu strictu*, but they are mica/smectite mixed-layer having more than 90% mica layers. They share with other glauconites the representative maximum K^+ content described up to now in the literature, but also their mixed-layer character (Fig. 8C).

In Figure 8C, the equation that relates % of glauconite layers of the interstratified glauconite-smectite mixed-layer with the interlayer K^+ (a.p.f.u.) content, build a logarithmic function model with an end-asymptotic behavior. The minimum K^+ content for a % of theoretical glauconite layers = 0, would be then 0.07 a.p.f.u., which in turn is reasonable with the common average K^+ content in smectitic layers; in other words, the K^+ content is not 0, since the smectitic layers also contain some potassium (Drief and Nieto, 2000). Furthermore, the curved trendline in Figure 8C never reaches values of K^+ content higher than 0.8 a.p.f.u., that is even for 100% of glauconite layers (the extreme term 'glauconitic mica') the K^+ content would be ~ 0.8 a.p.f.u. This is just the value used by the IMA in the 'representative formula' of glauconites and is neighboring its proposed maximum limit for interlayer-deficient micas (Rieder et al, 1998).

We conclude that the interlayer-deficient character accepted by the IMA and AIPEA nomenclature committees are due in part to the presence of interstratified smectitic layers, rather than barely an intrinsic chemical characteristic of the individual mica-packets constituents of the mixed-layer. This is also the reason why glauconites, even the more mature (evolved) ones, show a slight expansive character and basal reflection d_{001} located at some higher value than 10Å, as defined by the AIPEA. Therefore, glauconites should be broadly considered as mica-rich mica-smectite R3 interstratified minerals, having its specific well-known chemical composition. The corresponding 100%-mica extreme term should not occur in nature (at least in the usual glauconitic genetic contexts) and its K^+ content would be similar to 0.8 a.p.f.u.

IMPLICATIONS

In the present work, new insights into the nature of glauconite have been obtained by using a combined XRD, HRTEM and EPMA study. The studied mature glaucony grains consists of a glauconite-smectite (R3 ordered) mixed-layer silicate, composed mainly of mica-type layers (> 90%), but displaying slightly different proportions of interstratified Fe(III)-smectite layers (<10%). The smectite layers are responsible of the usually described change of the position of the d_{001} peak of glauconite after ethylene glycol treatment as far as, at least in part, their K-deficient character.

The smectite-to-glauconite reaction constitutes an evolutionary process monitored by K^+ increase at the interlayer sheet, as normally accepted, but also by the increase in Fe^{2+}/Fe^{3+}. More mature glaucony are characterized by major K^+ and $^{VI}Fe^{2+}$ (mica layers) and minor $^{VI}Fe^{3+}$ (smectite layers) contents in the interstratified glauconite-smectite, which indicates that K^+ is stabilized at the interlayer site by the octahedrally coordinated Fe^{2+} relative to the total ^{VI}Fe.

Glauconite is described here as mica-rich mica-smectite R3 interstratified mineral, with specific chemical composition. In addition, the theoretical end-member glauconitic mica would have an interlayer-deficient chemical characteristic with K^+ up to 0.8 a.p.f.u.

ACKNOWLEDGMENTS AND FUNDING

This research used samples from the Ocean Drilling Program (ODP). We thank the staff onboard ODP Leg 113 and at the Gulf Coast Repository (GCR) for assistance in core handling and shipping. We thank Dr. María del Mar Abad, Dr. Miguel Angel Hidalgo and Isabel Nieto of the Scientific Instrumentation Center (CIC) of the University of Granada for their help during analytical work. We would also like to thank Associate Editor Prof. Warren Huff and anonymous referees for their constructive

suggestions to improve the paper. Funding for this research was provided by the Spanish Ministry of Science and Innovation (grants CTM2014-60451-C2-1-P and CTM2017-89711-C2-1-P) co-funded by the European Union through FEDER funds. The corresponding author acknowledges a FPI fellowship of the Spanish Ministry of Science and Innovation.

REFERENCES CITED

Amorosi, A. (1995) Glaucony and sequence stratigraphy: a conceptual framework of distribution in siliciclastic sequences. Journal of Sedimentary Research 65, 419–425.

Amorosi, A. (2012) The occurrence of glaucony in the stratigraphic record: distribution patterns and sequence stratigraphic significance. International Association of Sedimentologists Special Publications 45, 37–54.

Amorosi, A., Sammartino, I. and Tateo, F. (2007) Evolution patterns of glaucony maturity: a mineralogical and geochemical approach. Deep-Sea Research Part II: Topical Studies in Oceanography 54, 1364–1374.

Amouric, M. (1990) La transformation gel smectite glauconite. In: Matériaux Agileux: Structure, Propriétés et Applications (A. Decarreau, editor). Societé Française de Minéralogie et Cristallographie, Paris, pp. 451–461.

Amouric, M. and Parron, C. (1985) Structure and growth mechanism of glauconite as seen by high-resolution transmission electron microscopy. Clays and Clay Minerals 33, 473–482.

Bailey, S.W. (1980) Summary of recommendations of AIPEA nomenclature committee. Clay and Clay Minerals 28 (1), 73–78.

496 Baldermann, A., Dietzel, M., Mavromatis, V., Mittermayr, F., Warr, L.N. and
497 Wemmer, K. (2017) The role of Fe on the formation and diagenesis of interstratified
498 glauconite-smectite and illite-smectite: A case study of Lower Cretaceous shallow-
499 water carbonates. Chemical Geology 453, 21–34.
500 Baldermann, A., Grathoff, G.H. and Nickel, C. (2012) Micromilieu-controlled
501 glauconitization in fecal pellets at Oker (Central Germany). Clay Minerals 47, 513–538.
502 Baldermann, A., Warr, L.N., Grathoff, G.H. and Dietzel, M. (2013) The rate and
503 mechanism of deep-sea glauconite formation at the Ivory Coast-Ghana marginal ridge.
504 Clays and Clay Minerals 61, 258–276.
505 Baldermann, A., Warr, L.N., Letofsky-Papst, I. and Mavromatis, V. (2015)
506 Substantial iron sequestration during green-clay authigenesis in modern deep-sea
507 sediments. Nature Geosciences 8 (11), 885–889.
508 Barker, P.F., Kennett, J.P., et al. (1988) Proceedings of the Ocean Drilling Program,
509 Initial Reports, 113. Ocean Drilling Program, College Station, Texas.
510 Bauluz, B. (2013) Clays in low-temperature environments. In: Minerals at the
511 nanoscale. Nieto, F. and Livi F.T. (eds.). EMU notes in Mineralogy, 14, 181–209.
512 Bauluz, B., Peacor, D.R. and González López, J.M. (2000) Transmission electron
513 microscopy study of illitization in pelites from the Iberian Range, Spain, layer-by-layer
514 replacement? Clays and Clay Minerals 48, 374–384.
515 Buatier, M., Honnorez, J. and Ehret, G. (1989) Fe-smectite-glauconite transition in
516 hydrothermal green clays from the Galapagos spreading center. Clays and Clay
517 Minerals 37, 532–541.
518 Burst, J.F. (1958) Mineral heterogeneity in glauconite pellets. American
519 Mineralogist 43, 481–49.
520 Chamley, H. (1989) Clay Sedimentology. Springer, Berlin.

Charpentier, D., Buatier, M.D., Jacquot, E., Gaudin, A. and Wheat, C.G. (2011) Conditions and mechanism for the formation of iron-rich montmorillonite in deep-sea sediments (Costa Rica margin); coupling high-resolution mineralogical characterization and geochemical modelling. Geochimica et Cosmochimica Acta 75, 1397–1410.

Coren, F., Ceccone, G., Lodolo, E., Zanolla, C., Zitellini, N., Bonazzi, C. and Centonze, J. (1997) Morphology, seismic structure and tectonic development of the Powell Basin, Antarctica. Journal of the Geological Society of London 154, 849–862

Deb, S.P. and Fukuoka, M. (1998) Fe-illites in a Proterozoic deep marine slope deposit in the Penganga Group of the Pranhita Godavari Valley: their origin and environmental significance. The Journal of Geology 106, 741–750.

Drief, A. and Nieto, F. (2000) Chemical composition of smectites formed in clastic sediments. Implications for the smectite-illite transformation. Clay Minerals 35, 665–678.

Duplay, J. and Buatier, M. (1990) The problem of differentiation of glauconite and celadonite. Chemical Geology 84, 264–266.

Eder, V.G., Martí -Algarra, A. Sá chez-Navas, A., Zanin, Y.N., Zamirailova, A.G., Lebedev, Y. (2007) Depositional controls on glaucony texture and composition, Upper Jurassic, West Siberia Basin. Sedimentology 54, 1365–1387.

Ehlmann, A., Hulings, N. and Glover, E. (1963) Stages of glauconite formation in modern foraminiferal sediments. Journal of Sedimentary Petrology 33, 87–96.

Galán, E., González, I., Mayoral, E. and Muniz, F. (1995) Contribution of clay mineralogy to the paleoenvironmental interpretation of upper miocene detrital sediments. Southwestern of the Iberian Peninsula. In: Euroclay'95, Book of Abstracts (A. Elsen, P. Grobet, M. Keung, H. Leeman, R. Schoonheydt and H. Toufar, editors), pp. 311–312.

546 Galliher, E.W. (1935) Glauconite genesis. Geological Society of America Bulletin,
547 46, 1351–1356.
548 Gaudin, A., Buatier, M.D., Beaufort, D., Petit, S., Grauby, O. and Decarreau, A.
549 (2005) Characterization and origin of Fe^{3+}-montmorillonite in deep-water calcareous
550 sediments (Pacific Ocean, Costa Rica Margin). Clays and Clay Minerals 53, 452–465.
551 Gersonde, R. and Burckle, L.H. (1990) Neogene Diatom biostratigraphy of ODP Leg
552 113, Weddell Sea Antarctic Ocean. In: Barker, P.F., Kennett J.P., et al., Proceeding of
553 the Ocean Drilling Program, Scientific Results, Leg 113,Volume 113: 761–789. College
554 Station, Texas: Ocean Drilling Program.
555 Guthrie, G. and Veblen, D. (1989) High-resolution transmission electron microscopy
556 of mixed-layer illite/smectite: Computer simulations. Clays and Clay Minerals 37, 1–11.
557 Guthrie, G. and Veblen, D. (1990) Interpreting one-dimensional high-resolution
558 transmission electron micrographs of sheet silicates by computer simulation. American
559 Mineralogist 75, 276–288.
560 Harder, H. (1980) Synthesis of glauconite at surface temperatures. Clays and Clay
561 Minerals 28, 217□–222.
562 Houben, A.J.P., Bijl, P.K., Pross, J., Bohaty, S.M., Passchier, S., Stickley, C.E., Röhl,
563 U., Sugisaki, S., Tauze, L., van de Flierdt, T., Olney, M., Sangiori, F., Sluijs, A.,
564 Escutia, C., Brinkhius, H. and the Expedition 318 Scientists (2013) Reorganization of
565 Southern Ocean plankton ecosystem at the onset of Antarctic Glaciation. Science 340,
566 341–344.
567 Hower, J. (1961) Some factors concerning the nature and origin of glauconite.
568 American Mineralogist 46, 313-334.
569 Huggett, J.M. (2005) Glauconites. Pp. 542–548 in: Encyclopedia of Geology (R.C.
570 Selley, L.R.M. Cocks, and I.R. Plimer, editors). Elsevier, Oxford.

Ireland, B.J., Curtis, C.D. and Whiteman, J.A. (1983) Compositional variation within some glauconites and illites and implications for their stability and origins. Sedimentology 30, 769–786.

Jiménez-Millán, J. and Castro, J.M. (2008) K-feldspar alteration to gel material and crystallization of glauconitic peloids with berthierine in Cretaceous marine sediments-sedimentary implications (Prebetic Zone, Betic Cordillera, SE Spain). Geological Journal 43(1), 19–31.

Jiménez-Millán, J., Molina, J.M., Nieto, J., Nieto, L. and Ruiz-Ortiz, P.A. (1998) Glauconite and phosphate peloids in Mesozoic carbonate sediments (Eastern Subbetic Zone, Betic Cordilleras, SE Spain). Clay Minerals 33, 547–559.

King, E.C. and Barker, P.F. (1988) The margins of the South Orkney microcontinent. Journal of the Geological Society of London 145, 317–331.

Kloprogge, J.T., Komarneni, S., and Amonette, J.E. (1999) Synthesis of smectite clay minerals: A critical review. Clays and Clay Minerals 47, 529–554.

Köster, H.M. (1982) The crystal structure of 2:1 layer silicates. Proceedings of the International Clay Conference, Bologna-Pavia, 41–71.

Köster, H.M., Ehrlicher, U., Gilg, H.A., Jordan, R., Murad, E., Onnich, K. (1999) Mineralogical and chemical characteristics of five nontronite and Fe-rich smectites. Clay Minerals 34, 579–599.

López-Quirós, A., Escutia, C., Sánchez-Navas, A., Nieto, F., García-Casco, A., Martín-Algarra, A., Evangelinos, D. and Salabarnada, A., submitted for publication. Glaucony authigenesis, maturity and alteration in the Weddell Sea: An indicator of paleoenvironmental conditions before the onset of Antarctic glaciation. Scientific Reports 9:13580; doi.org/10.1038/s41598-019-50107-1.

595 Lorimer, G.W. and Cliff, G. (1976) Analytical electron microscopy of minerals. In
596 Electron Microscopy in Mineralogy (H.-R. Wenk, ed.). Springer, Berlin, Germany
597 (506–519).
598 Manghnani, M.H., Hower, J. (1964) Glauconites: cation exchange capacities and
599 Infrared, Part II. Infrared absorption characteristics of glauconites. American
600 Mineralogist 49, 1631–1642.
601 Martín-Algarra, A. and Sánchez-Navas, A. (1995) Phosphate stromatolites from
602 condensed cephalopod limestones, Upper Jurassic, Southern Spain. Sedimentology 42,
603 893–919.
604 Martí -Algarra, A., Sá chez-Navas A. (2000) Bacterially mediated authigenesis in
605 Mesozoic stromatolites from condensed pelagic sediments (Betic Cordillera, Southern
606 Spain). In: Marine Authigenesis: From global to microbial (Glenn, C. R., Lucas, J. &
607 Prévôt-Lucas, L. eds.), S.E.P.M. Special Publication 66, 499–525.
608 McRae, S.G., Lambert, J.L.M. (1968) A study of some glauconites from Cretaceous
609 and Tertiary formations in South-East England. Clay Minerals 7, 431–440.
610 Meunier, A. and El Albani, A. (2007) The glauconite-Fe-illite-Fe- smectite problem:
611 a critical review. Terra Nova 19, 95–104.
612 Moore, D.M. and Reynolds, R.C. (1997) X-Ray Diffraction and the Identification
613 and Analysis of Clay Minerals: Oxford University Press, Oxford, 2nd ed., 378 p.
614 Nieto, F., Ortega-Huertas, M., Peacor, D., and Arostegui, J. (1996) Evolution of
615 illite/smectite from early diagenesis through incipient metamorphism in sediments of
616 the Basque-Cantabrian Basin. Clays and Clay Minerals 44, 304–323.
617 Odin, G.S. and Fullagar, P.D. (1988) Geological significance of the glaucony facies.
618 Green Marine Clays 45, 295–332.

Odin, G.S. and Létolle, R. (1980) Glauconitization and Phosphatization Environments: a Tentative Comparison. SEPM Special Publications 29, 227–237.

Odin, G.S. and Matter, A. (1981) De glauconiarum origine. Sedimentology 28 (5), 611–641.

Ojakangas R.W. and Keller W.D. (1964) Glauconitization of rhyolite sand grains. Journal of Sedimentary Petrology 34, 84–90.

Reolid, M., Abad, I. (2014) Glauconitic laminated crusts from hydrothermal alteration of Jurassic pillow-lavas (Betic Cordillera, S Spain): A microbial influence case. Journal of Iberian geology 40, 389–408.

Rieder, M., Cavazzini, G., Dyakonov, Y.S., Frank-Kamenetskii, V.A., Gottardi, G., Guggenheim, S., Koval, P.V., Müller , G., Neiva, A.M.R., Radoslovich, E.W., Robert, J.-L., Sassi, F.P., Takeda, H., Weiss, Z. and Wones, D.R. (1998) Nomenclature of the micas. The Canadian Mineralogist 36, 905–912.

Sánchez-Navas, A., Algarra, A.M., Eder, V., Reddy, B.J., Nieto, F. and Zanin, Y.N. (2008) Color, mineralogy and composition of Upper Jurassic West Siberian glauconite: useful indicators of paleoenvironment. The Canadian Mineralogist 46, 1545–1564.

Sánche -Navas, A., Martí -Algarra, A., Nieto, F. (1998) Bacterially-mediated authigenesis of clays in phosphate stromatolites. Sedimentology 45–3, 519–533.

Stille, P. and Clauer, N. (1994) The process of glauconitization: chemical and isotopic evidence. Contributions to Mineralogy and Petrology 117, 253–262.

Van der Pluijm, B.A., Lee, J.H., and Peacor, D.R. (1988) Analytical electron microscopy and the problem of potassium diffusion. Clays and Clay Minerals 36, 498-504.

642 Veblen, D.R., Guthrie Jr, G.D., Livi K.J.T. and Reynolds R.C. Jr. (1990) High-
643 resolution transmission electron microscopy and electron diffraction of mixed-layer
644 illite/smectite: Experimental results. Clays and Clays Minerals 38, 1–13.

645 Velde, B. (1992) Introduction to Clay Minerals. Chapman & Hall, London.

646 Velde, B., 2005. Green clay minerals. In: Treatise on Geochemistry, Volume 7,
647 Sediments, Diagenesis, and Sedimentary Rocks (F.T. Mackenzie, ed.), Elsevier,
648 Amsterdam, 309–324 pp.

649 Wei, W. and Wise, S.W. (1990) Middle Eocene to Pleistocene calcareous
650 nannofossils re- covered by Ocean Drilling Program Leg 113 in the Weddell Sea. In:
651 Proceedings of the Ocean Drilling Program, Scientific Results 113, vol. 188. Ocean
652 Drilling Program, College Station, Texas, pp. 639–666.

653 Wiewióra, A., Giresse, P., Petit, S. and Wilamowski, A. (2001) A deep-water
654 glauconitization process on the Ivory Coast–Ghana Marginal Ridge (ODP site 959):
655 determination of Fe^{3+}-rich montmorillonite in green grains. Clays and Clay Minerals 49
656 (6), 540–558.

657 Zanin, Y. N., Eder, V. G., Zamirailova, A. G. (2004) Bacterial forms in glauconites
658 from Upper Jurassic deposits of the West Siberian Plate. Russian Geology and
659 Geophysics 45, 774–777.

660 Giresse, P. and Wiewióra, A. (2001) Stratigraphic condensed deposition and
661 diagenetic evolution of green clay minerals in deep water sediments on the Ivory Coast-
662 Ghana Ridge. Marine Geology 179, 51–□70.

663 Giresse, P., Gadel, F., Serve, L., and Barusseau, J.P. (1998) Indicators of climate and
664 sediment-source variations at site 959: implications for the reconstructions of
665 paleoenvironments in the Gulf of Guinea through Pleistocene times. Proceedings of the
666 Ocean Drilling Program, Scientific Results 159, 585–603.

667 Odom, E. (1976) Microstructure, mineralogy and chemistry of Cambrian glauconite
668 pellets and glauconite, central USA. Clays and Clay Minerals 24, 232–238.
669 Strickler, M.E. and Ferrell, R.E. (1990) Fe substitution for Al in glauconite with
670 increasing diagenesis in the first Wilcox sandstone (Lower Eocene), Livingston Parish,
671 Lousiana. Clays and Clay Minerals 38, 69–76.
672

673 **FIGURE CAPTIONS**

674

675 **Figure 1.** Model for glauconitization in the studied grains (modified after López-Quirós
676 et al., 2019, following the ideas of Odin and Matter, 1981 and Baldermann et al., 2013).
677 **(1)** Microbial oxidation of organic matter (~10-10^3 years). **(2)** Neoformation of Fe(III)-
678 smectite precursor (~10^3-10^4 years). **(3)** Fe(III)-smectite-to-glauconite reaction (~10^4-
679 10^6 years). Glaucony maturation involves the chemical change of Si, Al^{VI}, Mg, Ca and
680 Na by Al^{IV}, Fe (Fe^{2+}) and K, from a smectitic glauconite (nascent) to the glauconitic
681 mica (highly evolved). Microtextures also attest glaucony maturation from authigenic
682 globules to flakes and rosettes.
683

684 **Figure 2. A)** Simplified bathymetry map of the Drake-Passage Scotia Sea area derived
685 from GEBCO. The squared region indicates the study area. **B)** Lithostratigraphy of the
686 Leg 113, ODP Site 696. The enlarger area corresponds with a detailed lithologic log of
687 the terrigeous to authigenic *Unit VII* (after Barker et al., 1988 and López-Quirós et al.,
688 2019). The studied glaucony grains come from two stratigraphic sections at cores 56-
689 57R and 51-52R, respectively. *OMT:* Oligocene-Miocene Transition. **C)** and **D)** Plain-
690 polarized light (PPL) images showing the glauconitic sandy-silty mudstone facies
691 (Subunits VIIC and VIIA, respectively). **E)** Back-scattered electron (BSE) image of a

692 reworked glaucony grain partially replaced by nontronite from core 52R. **F)** and **G)**
693 High-resolution transmission electron (HRTEM) images showing the characteristic
694 evolved (lamellar) microtexture of glaucony (cores 57R and 52R, respectively). **H)** BSE
695 image of a detailed evolved (cracked) glaucony grain from core 52R. **I)** Secondary
696 electron (SE) image showing the evolved morphology (cracked grains) and
697 microtexture (flaky/lamellar) of glauconitized pellets from core 57R.
698
699 **Figure 3. A)** Powder X-ray diagram of air-dried and ethylene-glycol-treated glaucony
700 from core 57R. **B)** Deconvoluted (001) peak at ~10Å of ethylene-glycol-treated
701 glaucony from core 57R. **C)** Powder X-ray diagram of air-dried and ethylene-glycol-
702 treated glaucony from core 52R. **D)** Deconvoluted (001) peak at ~10Å of ethylene-
703 glycol-treated glaucony from core 52R. Theoretical curves (bold lines in deconvoluted
704 diagrams), resulting from the sum of the deconvoluted peaks (blue, red and orange
705 lines), display good agreement with experimental diagrams. Red and orange peaks
706 correspond to R3 illite(0.9)/smectite (see for more details Fig. 4A) and blue peak to
707 smectite or smectite-rich R0 illite/smectite.
708
709 **Figure 4. A)** Deconvoluted (001) peak at ~10Å of ethylene-glycol-treated glaucony
710 from core 56R with corresponding residue and peak list. Theoretical curve (bold line),
711 resulting from the sum of the glycolated peaks at ~18Å, ~11A°, ~10A° and ~9Å, display
712 good agreement with experimental diagram (in red). **B)** Theoretical simulated powder
713 X-ray diagram of air-dried and ethylene-glycol-treated R3 illite(0.9)/smectite, with the
714 indication of *d*-values (adapted from the Fig. 8.7 of Moore and Reynolds, 1997).
715

716 **Figure 5. A)** HRTEM image of glaucony crystals from core 57R. False color map
717 displays the mineral nature, in order to emphasize the glauconite-smectite mixed-layer.
718 Enlarged circle shows the selected-area electron diffraction (SAED) pattern of the
719 correspondig area in the HRTEM image. **B)** Enlarged area from (A) showing well-
720 defined ~10Å lattice fringes of glauconite crystal and two areas of interstratified
721 smectitic material. **C)** Energy-dispersive X-ray (EDX) spectrum of corresponding
722 interstratified glauconite-smectite crystal, obtained in STEM mode from a
723 compositional map (not shown). **D)** HRTEM image of glaucony crystals from core 52R.
724 False color also shows the mineral nature. Enlarged circle displays the SAED pattern of
725 correspondig area in the HRTEM image. **E)** Enlarged area from (D) showing well-
726 defined ~10Å lattice fringes of glauconite crystal and related interstratified smectitic
727 area. **F)** Well-defined ~10Å lattice fringes of glauconite crystals from core 52R.
728
729 **Figure 6.** Bivariate plots of ODP Hole 696B glaucony grains (data from Tables 2 and 3).
730 **A)** K^+ *vs.* $^{IV}Si^{4+}$; **B)** K^+ *vs.* $^{VI}Al^{3+}$; **C)** K^+ *vs.* $^{VI}Fe^{3+} + {}^{VI}Fe^{2+}$; **D)** K^+ *vs.* $^{VI}Fe^{2+}$, **E)** $^{VI}Fe^{3+}$
731 *vs.* $^{VI}Fe^{2+}$; **F)** $^{VI}Al^{3+}$ *vs.* $^{VI}Fe^{3+} + {}^{VI}Fe^{2+}$.
732
733 **Figure 7. A)** Charge-distribution diagram with end-members celadonite, muscovite, and
734 pyrophyllite (modified from Köster, 1982; Köster et al., 1999). G: glauconite domain,
735 M: montmorillonite domain, N: nontronite and beidellite domain, C: celadonite domain.
736 Note that the analyzed glaucony plots in the field of glauconite domain. **B)** Position of
737 ODP Hole 696B glaucony (Tables 2 and 3 for more information) in the compositional
738 diagram of Fe-bearing clay phases in the $M^+ \cdot (Si/4)^{-1}$ *vs.* $^{VI}Fe(II+III)/\Sigma^{VI}$cations cross-
739 plot (modified after Meunier and El Albani, 2007). *MLM:* mixed-layer minerals; M^+*:*
740 interlayer charge.

741

742 **Figure 8. A)** and **B)** Relationship between %glauconite and interlayer K^+ (a.p.f.u.)
743 content in the interstratified glauconite-smectite (GL-Sm) mixed-layers from ODP Hole
744 696B cores 57R and 52R, respectively. Note that expandable layers (%glauconite ~95 ±
745 5) are determined by XRD, while interlayer K^+ (a.p.f.u.) content is from results of
746 EPMA. **C)** Relationship between expandable layer (%glauconite layers) and interlayer
747 K^+ content in the interstratified GL-Sm mixed layer (modified after Baldermann et al.
748 2013). Average position of ODP Hole 696B glaucony from cores 57R and 52R along
749 with values from other glaucony-bearing sequences (including those incorporated in Fig.
750 11 of Baldermann et al., 2013) has been included. Calculated logarithmic trendline with
751 end-asymptotic behavior in red color.

752

753 **TABLE CAPTIONS**

754

755 **Table 1.** Selected results of AEM [1]calculated chemical analyses of glaucony grains in
756 core 57R. [1]Units: atoms per formula unit (a.p.f.u.) based on $O_{10}(OH)_2$. *Total Fe
757 expressed as Fe^{3+}. *M*: octahedrally coordinated cations; *A*: interlayer cations.

758

759 **Table 2.** Results of EPMA [1]calculated chemical analyses for glaucony samples from
760 thin section (core 57R) (adapted from López-Quirós et al., 2019). [1]Units: atoms per
761 formula unit (a.p.f.u.). TC = tetrahedral charge, OC = octahedral charge; IC = interlayer
762 charge. Normalization to 2 octahedral + 4 tetrahedral cations and 22 charges (10 O+2
763 OH). †Fe^{2+} and Fe^{3+} in the formula calculated by stoichiometry.

764

765 **Table 3.** Results of EPMA [1]calculated chemical analyses for glaucony samples from
766 thin section (core 52R). [1]Units: atoms per formula unit (a.p.f.u.). TC = tetrahedral
767 charge, OC = octahedral charge; IC = interlayer charge. Normalization to 2 octahedral +
768 4 tetrahedral cations and 22 charges (10 O+2 OH). †Fe^{2+} and Fe^{3+} in the formula
769 calculated by stoichiometry.

Table 1. Selected results of AEM [1]calculated chemical analyses of glaucony grains in core 57R. [1]Units: atoms per formula unit (a.p.f.u.) based on $O_{10}(OH)_2$. *Total Fe expressed as Fe^{3+}. *M*: octahedrally coordinated cations; *A*: interlayer cations.

Sample	**1**	**2**	**3**	**4**	**5**	**6**	**7**	**8**	**9**	**10**
Si	3,64	3,71	3,82	3,74	3,81	3,82	3,79	3,77	3,69	3,66
^{IV}Al	0,43	0,46	0,43	0,39	0,38	0,4	0,51	0,43	0,42	0,41
Σ^{IV}	4	4	4	4	4	4	4	4	4	4
Ti	0,01	0,01	0,01	0,01	0,01	0,01	0,01	0,01	0,01	0,01
^{VI}Al	0,07	0,17	0,25	0,13	0,19	0,22	0,3	0,2	0,11	0,07
Fe*	1,57	1,48	1,31	1,51	1,4	1,35	1,32	1,45	1,55	1,58
Mg	0,34	0,34	0,43	0,36	0,38	0,41	0,35	0,34	0,32	0,36
Σ^{VI}*M*	1,99	2	2	2,01	1,98	1,99	1,98	2	1,99	2,02
Ca	0,05	0,05	0,04	0,05	0,03	0,05	0,04	0,04	0,04	0,05
K	0,6	0,55	0,53	0,51	0,56	0,53	0,54	0,51	0,58	0,58
Σ^{XII}*A*	0,65	0,6	0,57	0,56	0,59	0,58	0,58	0,55	0,62	0,63

Table 2. Results of EPMA [1]calculated chemical analyses for glaucony samples from thin section (core 57R) (adapted from López-Quirós et al. 2019). [1]Units: atoms per formula unit (a.p.f.u.). TC = tetrahedral charge, OC = octahedral charge; IC = interlayer charge. Normalization to 2 octahedral + 4 tetrahedral cations and 22 charges (10 O+2 OH). *Total Fe expressed as Fe^{3+}; † Fe^{2+} and Fe^{3+} in the formula calculated by stoichiometry.

Atoms per half-formula unit (a.p.f.u.) based on $O_{10}(OH)_2$

Substratum	T.1	T.1	T.1	T.1	T.1	T.1	T.1	T.1	T.1	T.1	T. 2	T. 2	T. 2	T. 2	T. 2	T. 2	T. 2	T. 2	Mica	Mica
Si	3,85	3,88	3,83	3,86	3,87	3,83	3,83	3,91	3,86	3,85	3,82	3,72	3,87	3,83	3,73	3,87	3,88	3,83	3,74	3,78
^{IV}Al	0,15	0,12	0,17	0,14	0,13	0,17	0,17	0,09	0,14	0,15	0,18	0,28	0,13	0,17	0,26	0,13	0,12	0,17	0,26	0,22
Σ^{IV}	4	4	4	4	4	4	4	4	4	4	4	4	4	4	4	4	4	4	4	4
TC	-0,15	-0,12	-0,17	-0,14	-0,13	-0,17	-0,17	-0,09	-0,14	-0,15	-0,18	-0,28	-0,13	-0,17	-0,26	-0,13	-0,12	-0,17	-0,26	-0,22
Ti	0,01	0,01	0,01	0,01	0,01	0,01	0,02	0,01	0,01	0,01	0,01	0,03	0,01	0,03	0,01	0,01	0,01	0,01	0,01	0,02
^{VI}Al	0,08	0,11	0,04	0,15	0,14	0,08	0,13	0,2	0,12	0,1	0,12	0,13	0,11	0,17	0	0,14	0,15	0,1	0,1	0,07
†Fe^{3+}	1,3	1,25	1,39	1,26	1,29	1,31	1,28	1,18	1,27	1,33	1,28	1,3	1,29	1,23	1,45	1,24	1,25	1,37	1,36	1,36
†Fe^{2+}	0,28	0,29	0,21	0,21	0,23	0,25	0,22	0,27	0,24	0,22	0,21	0,21	0,24	0,25	0,21	0,27	0,26	0,2	0,16	0,21
Mn	0	0	0	0	0	0	0	0	0	0	0	0	0	0	0	0	0	0	0	0
Mg	0,34	0,34	0,36	0,35	0,33	0,34	0,36	0,34	0,36	0,33	0,38	0,33	0,36	0,32	0,33	0,34	0,34	0,33	0,37	0,35
Σ^{VI}	2	2	2	2	2	2	2	2	2	2	2	2	2	2	2	2	2	2	2	2
OC	-0,58	-0,62	-0,53	-0,61	-0,55	-0,61	-0,53	-0,6	-0,59	-0,57	-0,58	-0,51	-0,56	-0,54	-0,53	-0,6	-0,56	-0,49	-0,52	-0,51
Ca	0,02	0,02	0,03	0,01	0,03	0,02	0,02	0,03	0,02	0	0,02	0,01	0,02	0,02	0,02	0,02	0,02	0,02	0,01	0,01
Na	0,01	0,01	0,01	0,01	0,01	0,01	0,01	0,01	0,01	0,02	0,01	0,01	0,01	0,01	0,01	0,01	0,01	0,02	0,01	0,01
K	0,7	0,7	0,66	0,67	0,62	0,71	0,67	0,62	0,67	0,67	0,71	0,75	0,67	0,66	0,75	0,68	0,66	0,63	0,74	0,72
Σ^{XII}	0,72	0,73	0,7	0,69	0,66	0,74	0,71	0,66	0,7	0,69	0,74	0,78	0,7	0,7	0,78	0,72	0,69	0,67	0,76	0,74
IC	0,75	0,75	0,73	0,7	0,69	0,76	0,72	0,69	0,72	0,69	0,76	0,78	0,72	0,71	0,8	0,73	0,71	0,69	0,77	0,75

Types: T.1 (type 1) and **T.2** (type 2) (EPMA results from López-Quirós et al., 2019)
TC = tetrahedral charge, OC = octahedral charge; IC = interlayer charge

Table 3. Results of EPMA [1]calculated chemical analyses for glaucony samples from thin section (core 52R). [1]Units: atoms per formula unit (a.p.f.u.). TC = tetrahedral charge, OC = octahedral charge; IC = interlayer charge. Normalization to 2 octahedral + 4 tetrahedral cations and 22 charges (10 O+2 OH). *Total Fe expressed as Fe^{3+}; † Fe^{2+} and Fe^{3+} in the formula calculated by stoichiometry.

Atoms per half-formula unit (a.p.f.u.) based on $O_{10}(OH)_2$

Substratum	Pellet	Pellet	Pellet	Pellet	Pellet	Pellet	Pellet	Pellet	Pellet	Pellet	Pellet	Diatom	Diatom	Diatom	Diatom	Mica	Mica
Si	3,84	3,84	3,86	3,85	3,86	3,86	3,83	3,81	3,84	3,85	3,86	3,86	3,86	3,86	3,89	3,79	3,85
^{IV}Al	0,16	0,16	0,14	0,15	0,14	0,14	0,17	0,19	0,16	0,15	0,14	0,14	0,14	0,14	0,11	0,21	0,15
Σ^{IV}	4	4	4	4	4	4	4	4	4	4	4	4	4	4	4	4	4
TC	-0,16	-0,16	-0,14	-0,15	-0,14	-0,14	-0,17	-0,19	-0,16	-0,15	-0,14	-0,14	-0,14	-0,14	-0,11	-0,21	-0,15
Ti	0,02	0,02	0,02	0,02	0,01	0,03	0,01	0,02	0,02	0,01	0,03	0,03	0,02	0,03	0,03	0,01	0,02
^{VI}Al	0,12	0,09	0,08	0,04	0,06	0,11	0	0,02	0,01	0,08	0,06	0,1	0,08	0,08	0,13	0,33	0,33
†Fe^{3+}	1,29	1,32	1,29	1,36	1,34	1,28	1,39	1,36	1,35	1,34	1,29	1,29	1,29	1,31	1,22	1,15	1,11
†Fe^{2+}	0,14	0,12	0,15	0,11	0,13	0,12	0,16	0,13	0,17	0,12	0,18	0,12	0,15	0,12	0,17	0,09	0,15
Mn	0	0	0	0	0	0	0	0	0	0	0	0	0	0	0	0	0
Mg	0,44	0,46	0,46	0,47	0,46	0,46	0,43	0,46	0,45	0,45	0,44	0,46	0,45	0,45	0,44	0,41	0,39
Σ^{VI}	2	2	2	2	2	2	2	2	2	2	2	2	2	2	2	2	2
OC	-0,53	-0,53	-0,59	-0,56	-0,58	-0,55	-0,61	-0,6	-0,6	-0,56	-0,59	-0,55	-0,61	-0,57	-0,61	-0,52	-0,52
Ca	0,03	0,03	0,03	0,03	0,03	0,03	0,03	0,02	0,02	0,02	0,03	0,03	0,03	0,03	0,03	0,03	0,03
Na	0,01	0,01	0,01	0,01	0,01	0,01	0,01	0,01	0,01	0,01	0,01	0,01	0,01	0,01	0,01	0,01	0,01
K	0,66	0,66	0,67	0,65	0,66	0,62	0,68	0,69	0,71	0,65	0,67	0,62	0,66	0,63	0,63	0,63	0,61
Σ^{XII}	0,7	0,7	0,71	0,69	0,69	0,66	0,72	0,73	0,74	0,68	0,71	0,66	0,69	0,67	0,67	0,67	0,65
IC	0,73	0,73	0,74	0,72	0,73	0,69	0,75	0,74	0,76	0,7	0,74	0,69	0,73	0,7	0,7	0,7	0,68

TC = tetrahedral charge, OC = octahedral charge; IC = interlayer charge

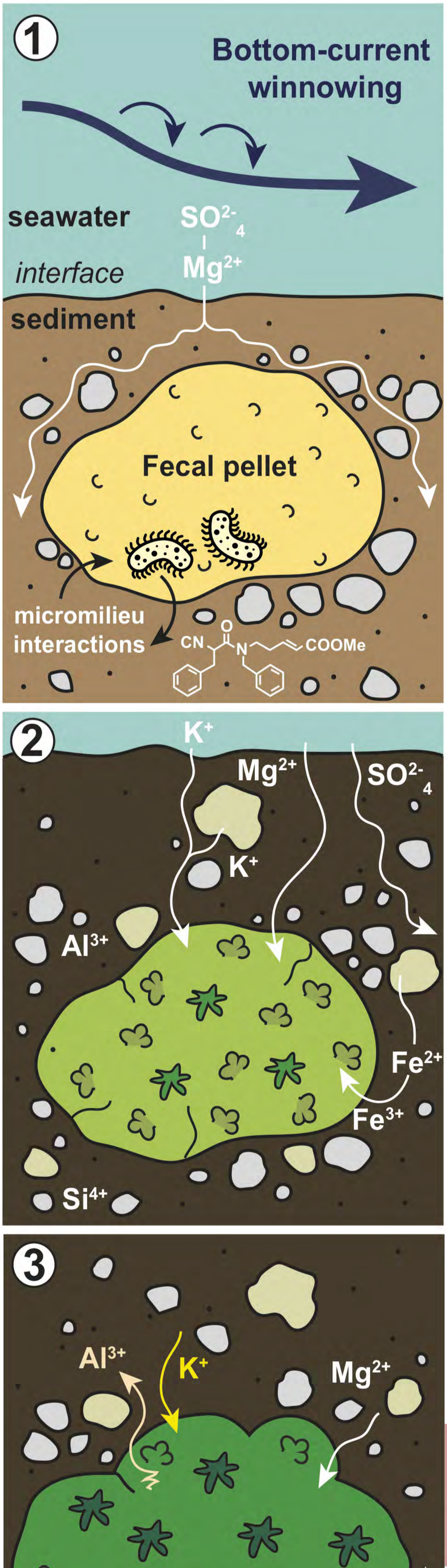
1
Bottom-current winnowing
seawater
SO^{2-}_4
Mg^{2+}
interface
sediment
Fecal pellet
micromilieu interactions
CN
O
N
COOMe
2
K^+
Mg^{2+}
SO^{2-}_4
K^+
Al^{3+}
Fe^{2+}
Fe^{3+}
Si^{4+}
3
Al^{3+}
K^+
Mg^{2+}
Fe^{2+}
Fe^{3+}
$+H_2S$
Si^{4+}
Glauconitic mica
'True glauconite'

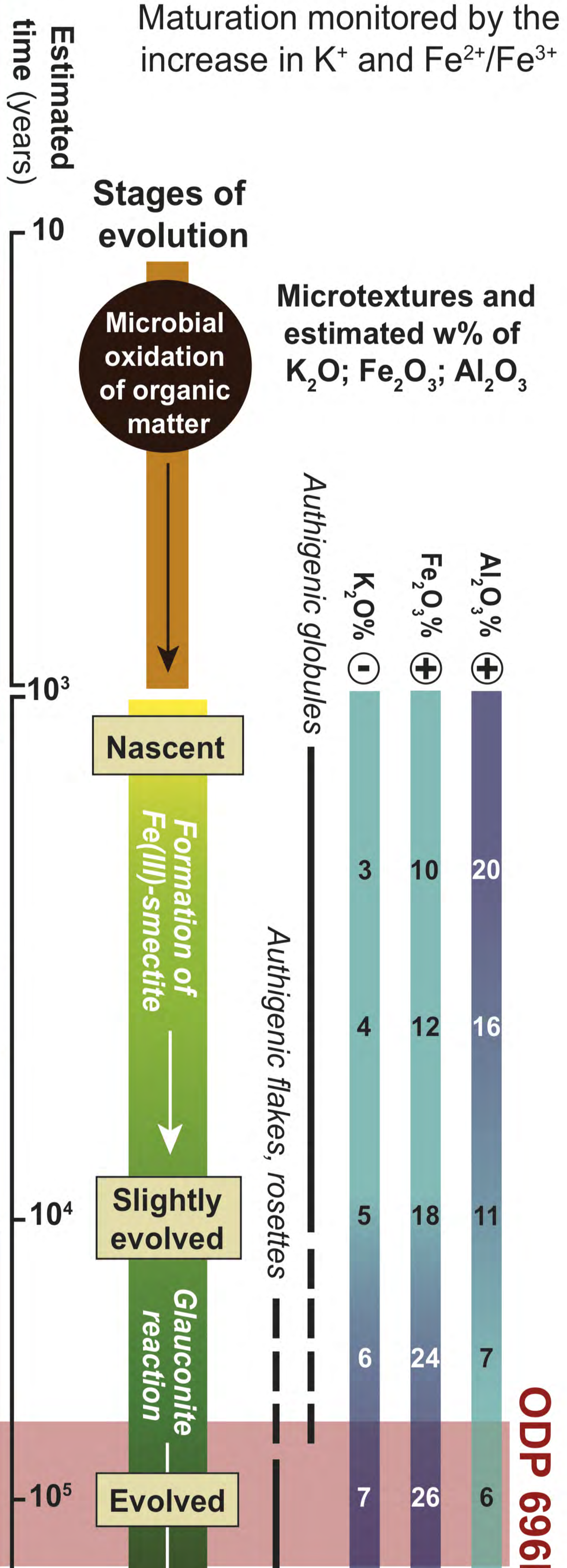
Maturation monitored by the increase in K^+ and Fe^{2+}/Fe^{3+}
Estimated time (years)
Stages of evolution
Microbial oxidation of organic matter
Microtextures and estimated w% of K_2O; Fe_2O_3; Al_2O_3
10^3
Nascent
Formation of Fe(III)-smectite
10^4
Slightly evolved
Glauconite reaction
10^5
Evolved
10^6
Highly evolved
Authigenic globules
Authigenic flakes, rosettes
Al_2O_3% ⊕
Fe_2O_3% ⊕
K_2O% ⊖
3 4 5 6 >8
10 12 18 24 26 28
20 16 11 7 6 8
⊕ ⊕ ⊖
ODP 696B

Figure 1

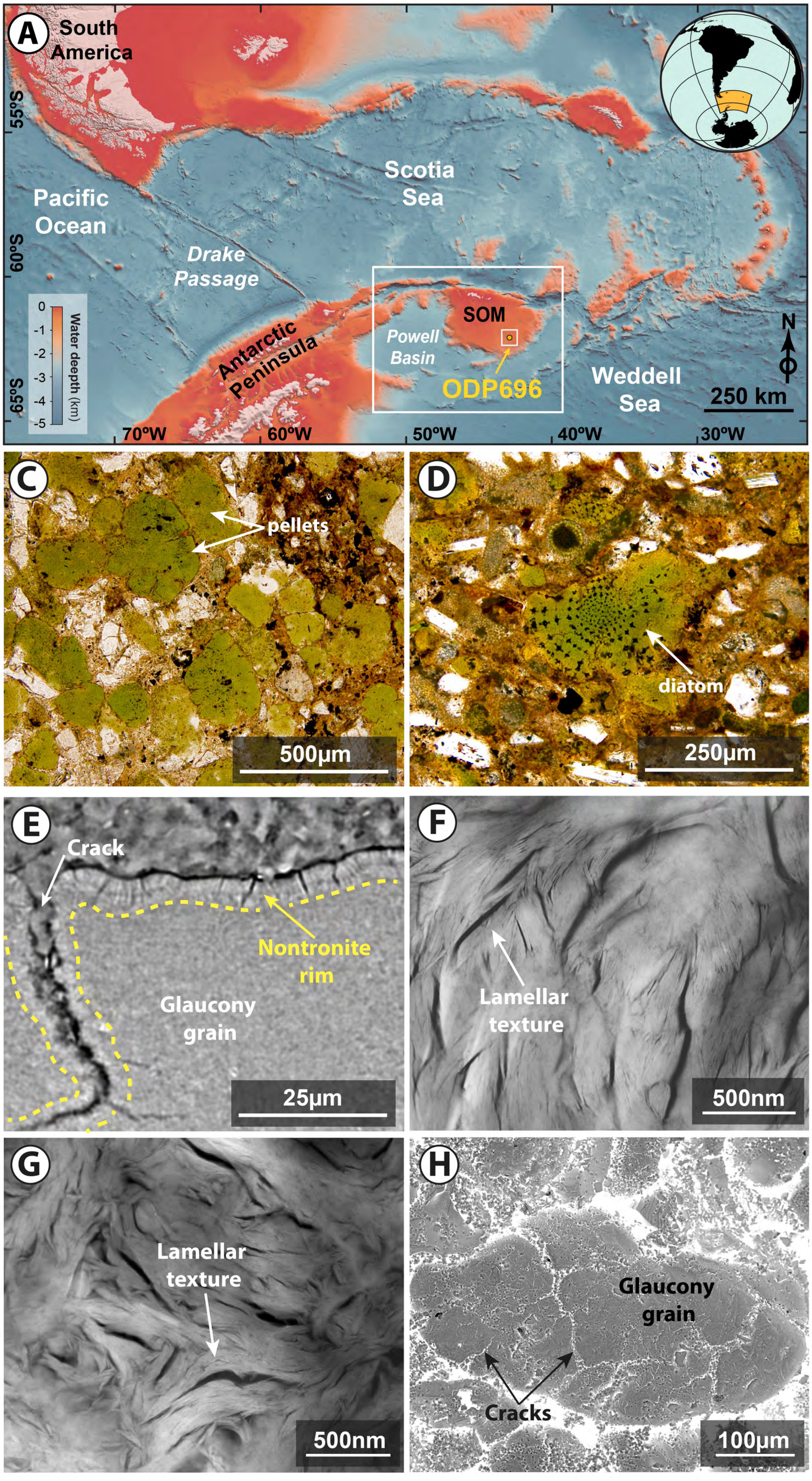
A
South America
Pacific Ocean
Scotia Sea
Drake Passage
Antarctic Peninsula
Powell Basin
SOM
ODP696
Weddell Sea
Water deepth (km)
0
-1
-2
-3
-4
-5
55°S
60°S
65°S
70°W
60°W
50°W
40°W
30°W
N
250 km
B
Lithostratigraphy
Chert
Diatom ooze/ diatomite
Grey clayey mudstone
Glauconitic sandy-silty mudstone
Organic-rich sandy mudstone
ODP 696
Core
Recovery
Age
Units
Lithology
Unit I
Unit II
Unit III
Unit IV
Unit V
Unit VI
Unit VII
0
211.8
529.8
645.6
Hemipelagic
Diatomaceous
Terrigenous
M. Mio.
Olig./Mio.
early Oligocene
late Eocene
Sub. VIB
Sub. VIIA
Subunit VIIB
Subunit VIIC
Subunit VIID
50R
51R
52R
53R
54R
55R
56R
57R
58R
59R
60R
61R
62R
520
530
540
550
560
570
580
590
600
610
620
630
640
Depth (mbsf)
C
pellets
500µm
D
diatom
250µm
E
Crack
Nontronite rim
Glaucony grain
25µm
F
Lamellar texture
500nm
G
Lamellar texture
500nm
H
Glaucony grain
Cracks
100µm
I
Evolved glaucony
Flaky/lamellar nanostructure
200µm

Figure 2

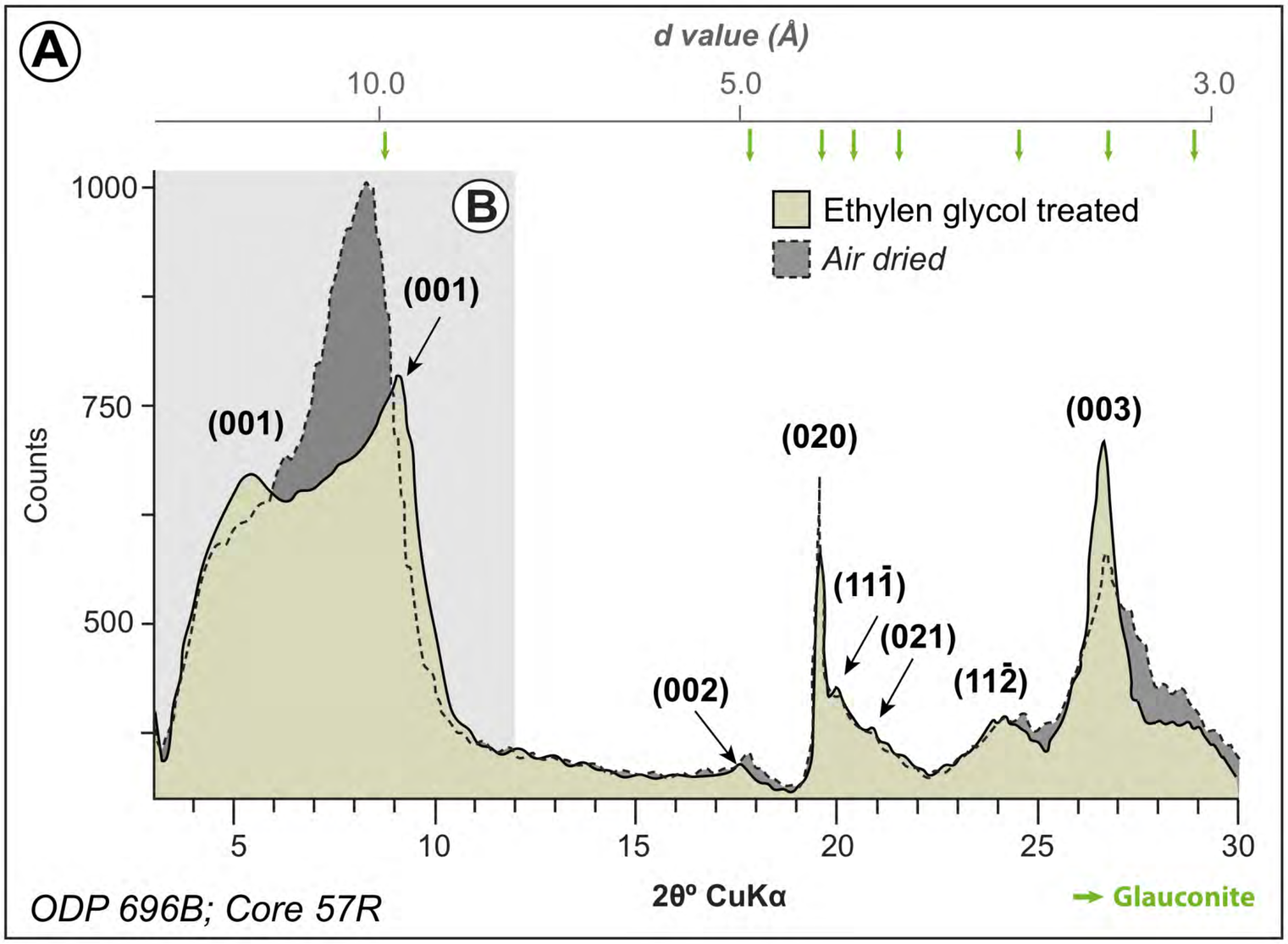
A
d value (Å)
10.0
5.0
3.0
B
Ethylen glycol treated
Air dried
(001)
(001)
(020)
(003)
(11$\bar{1}$)
(021)
(002)
(11$\bar{2}$)
Counts
2θº CuKα
Glauconite
ODP 696B; Core 57R

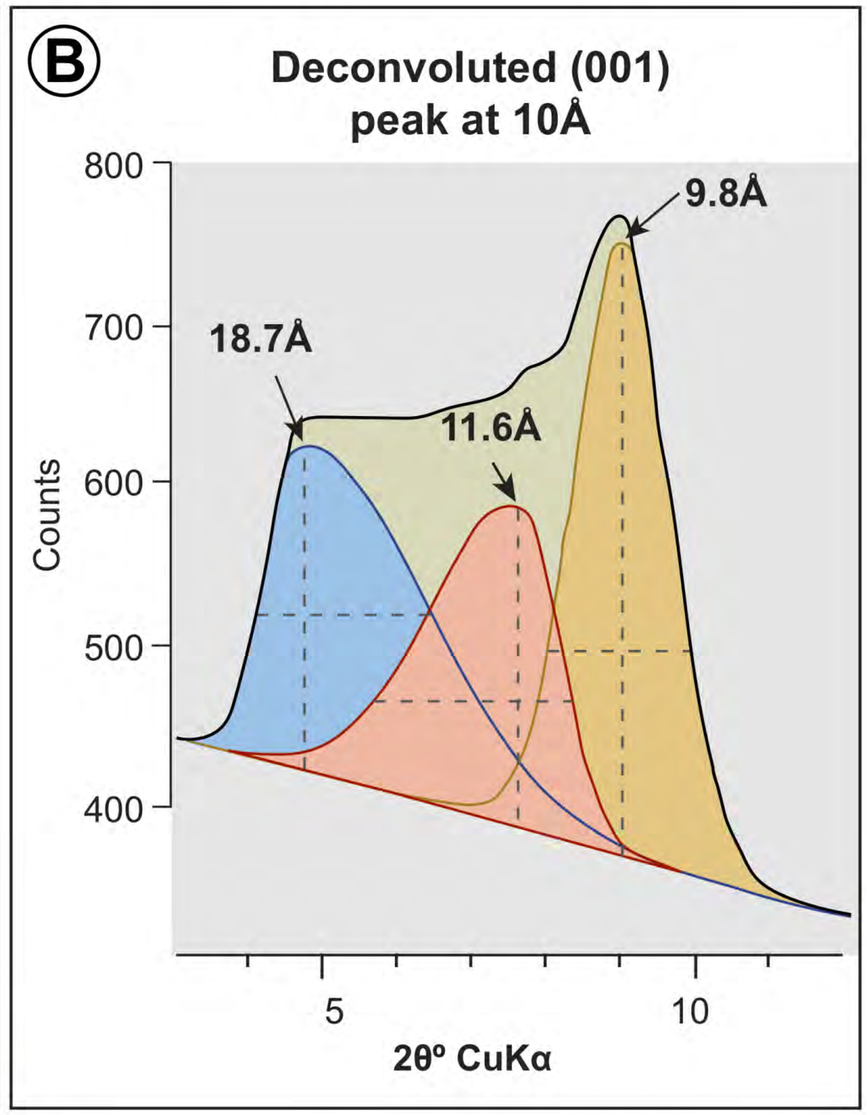
B
Deconvoluted (001)
peak at 10Å
9.8Å
18.7Å
11.6Å
Counts
2θº CuKα

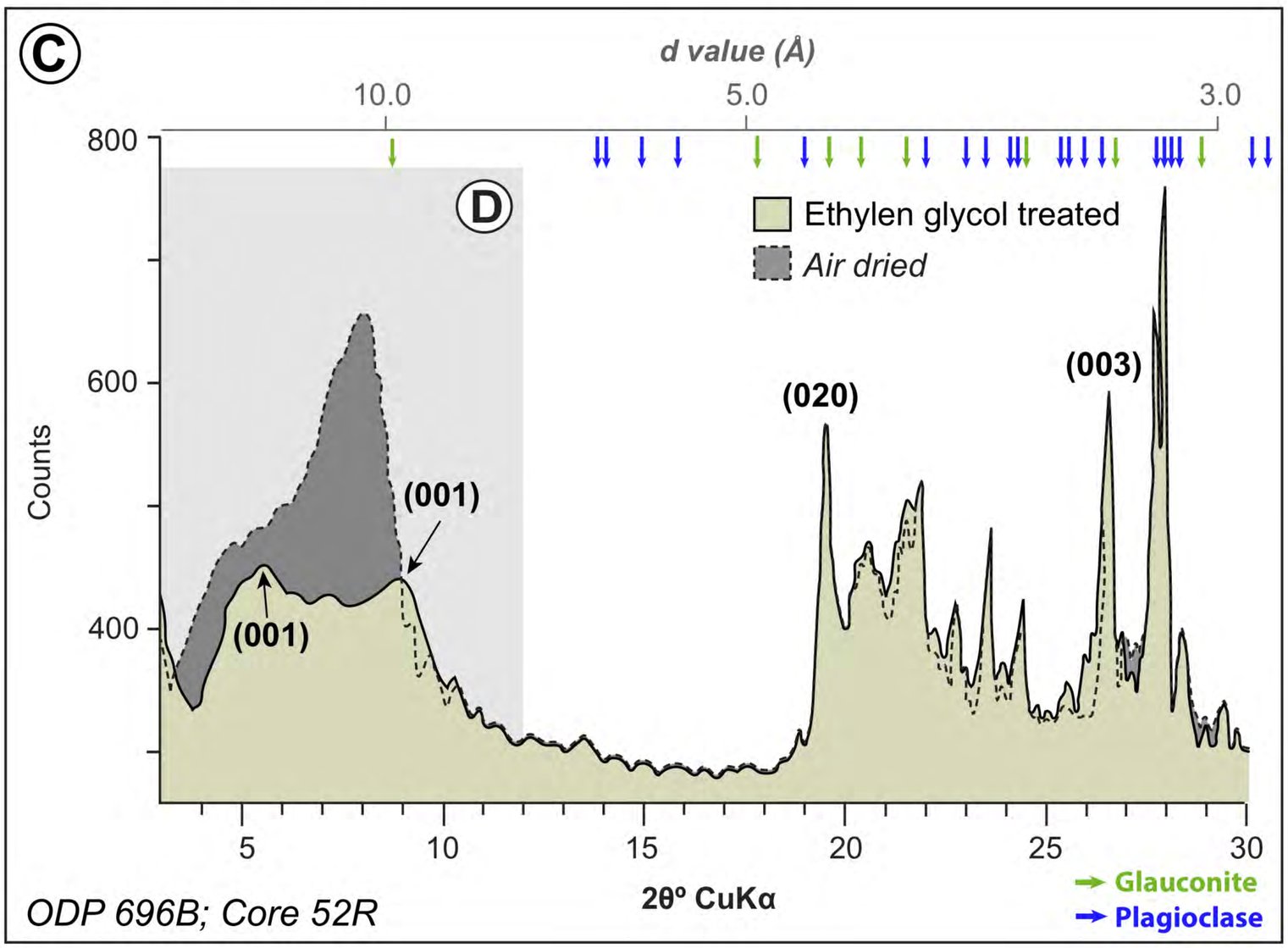
C
d value (Å)
10.0
5.0
3.0
D
Ethylen glycol treated
Air dried
(001)
(001)
(020)
(003)
Counts
2θº CuKα
Glauconite
Plagioclase
ODP 696B; Core 52R

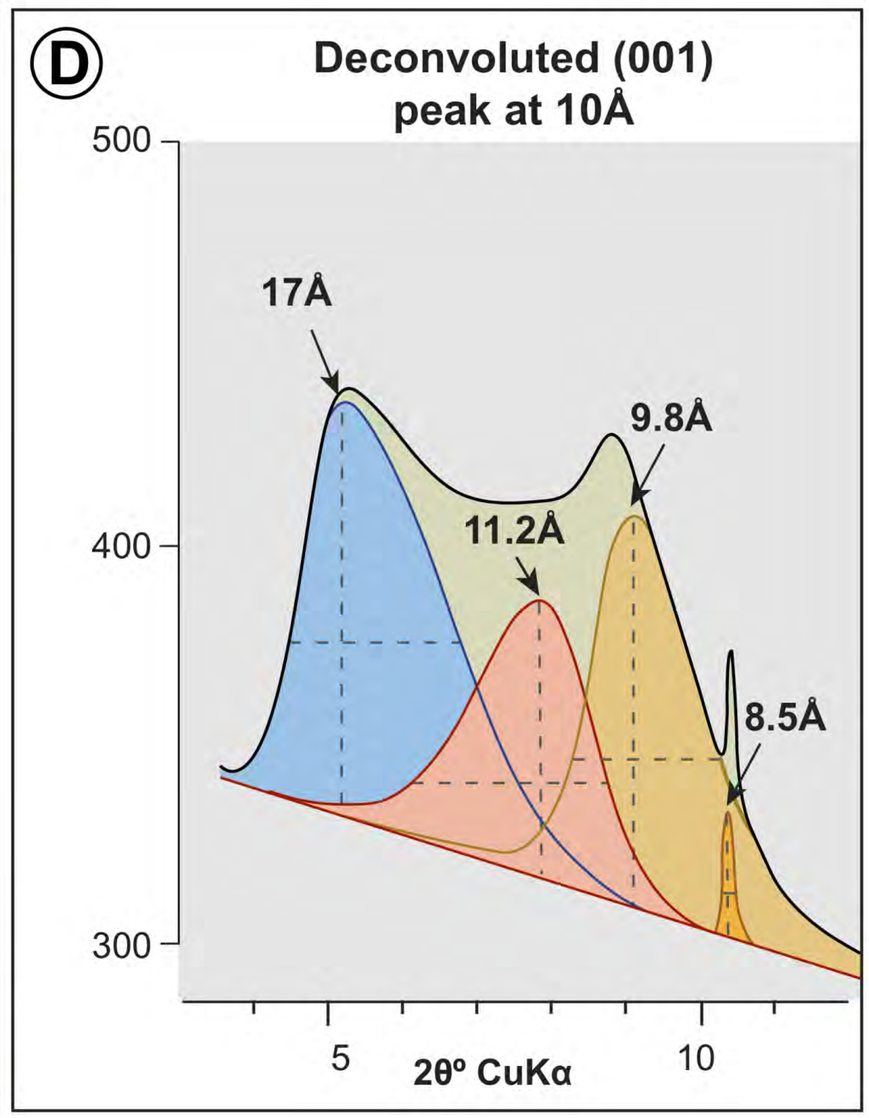
D
Deconvoluted (001)
peak at 10Å
17Å
9.8Å
11.2Å
8.5Å
2θº CuKα

Figure 3

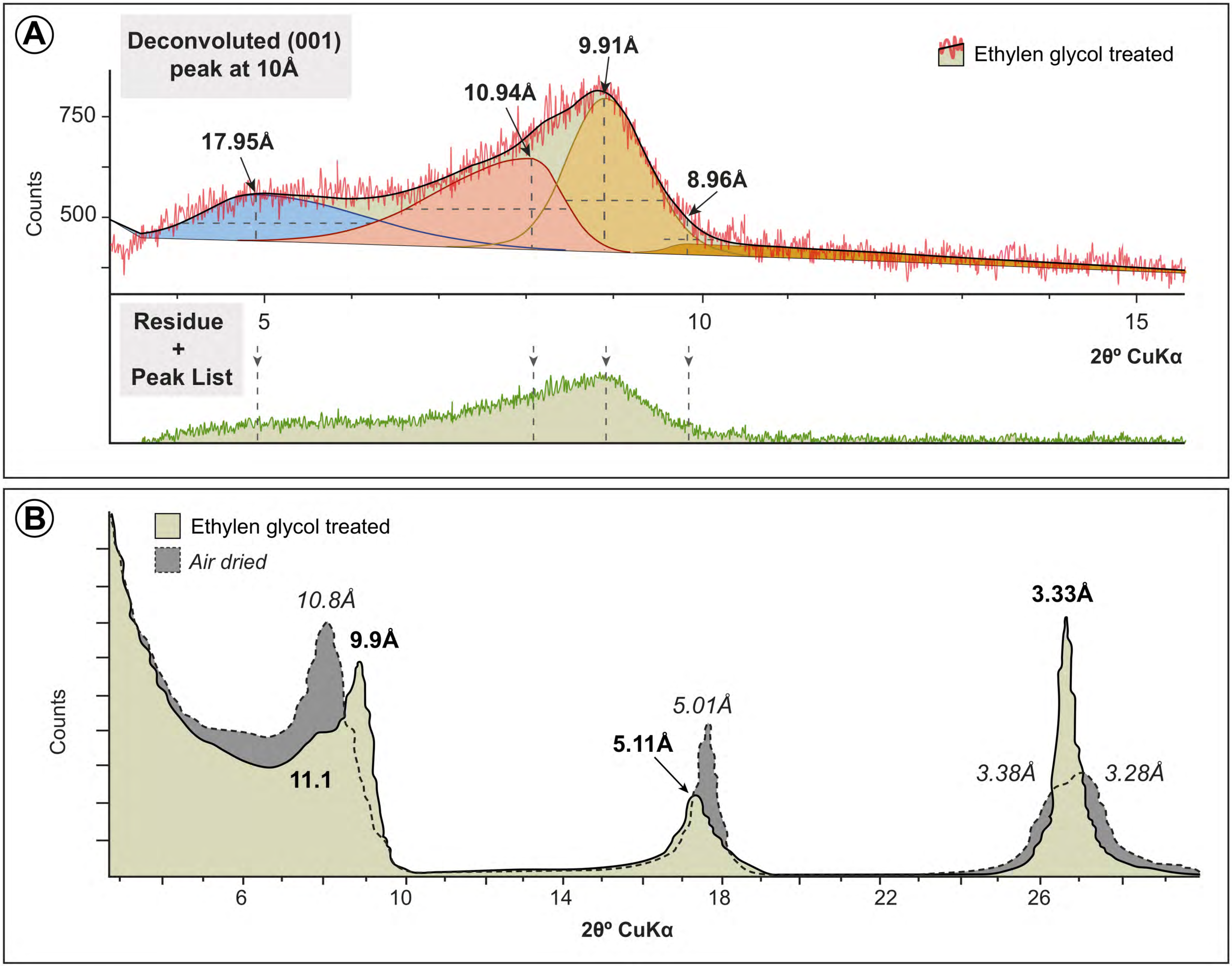
A
Deconvoluted (001) peak at 10Å
Ethylen glycol treated
9.91Å
10.94Å
17.95Å
8.96Å
750
500
Counts
Residue + Peak List
5
10
15
2θº CuKα
B
Ethylen glycol treated
Air dried
10.8Å
9.9Å
11.1
5.01Å
5.11Å
3.33Å
3.38Å
3.28Å
Counts
6
10
14
18
22
26
2θº CuKα

Figure 4

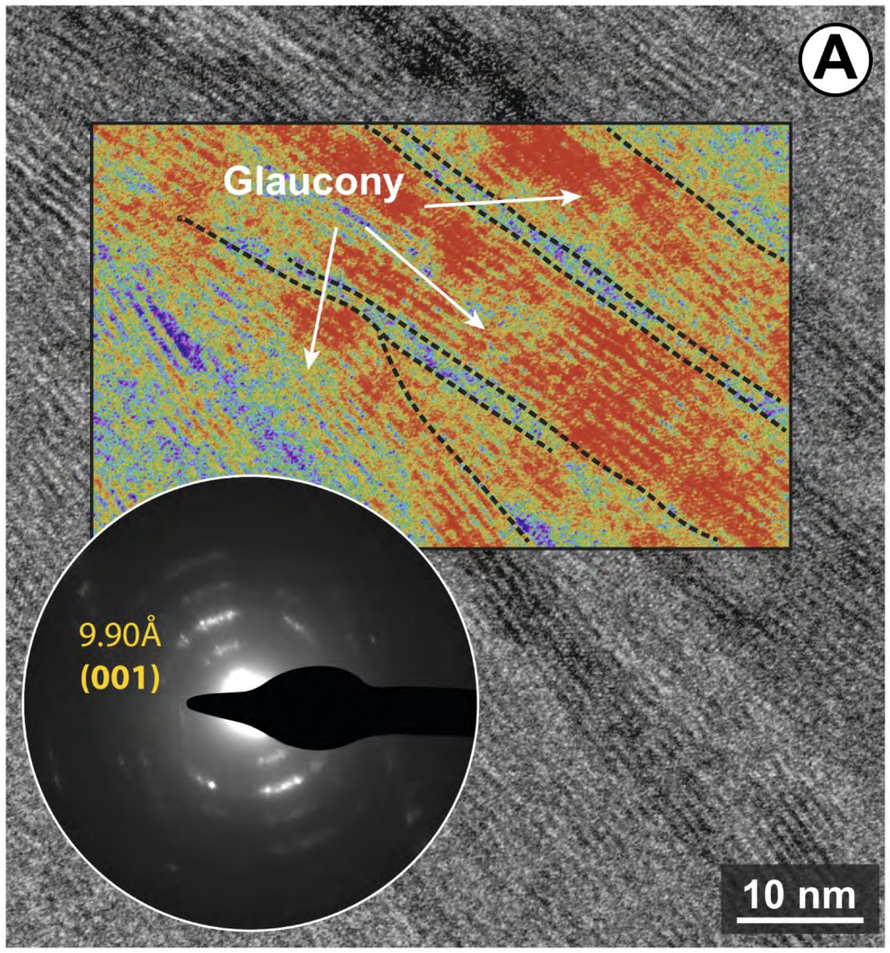
A
Glaucony
9.90Å
(001)
10 nm

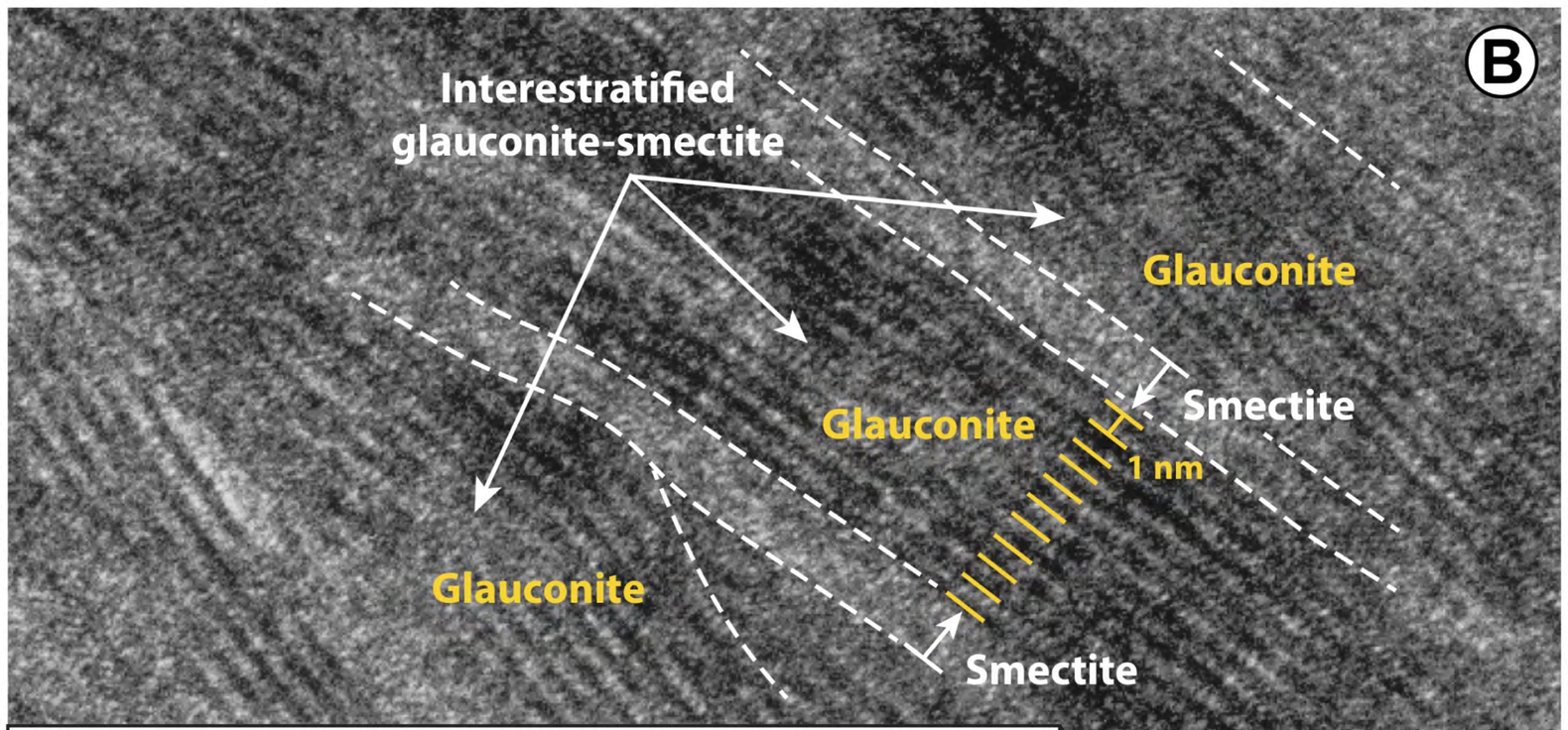
B
Interestratified
glauconite-smectite
Glauconite
Smectite
Glauconite
1 nm
Glauconite
Smectite

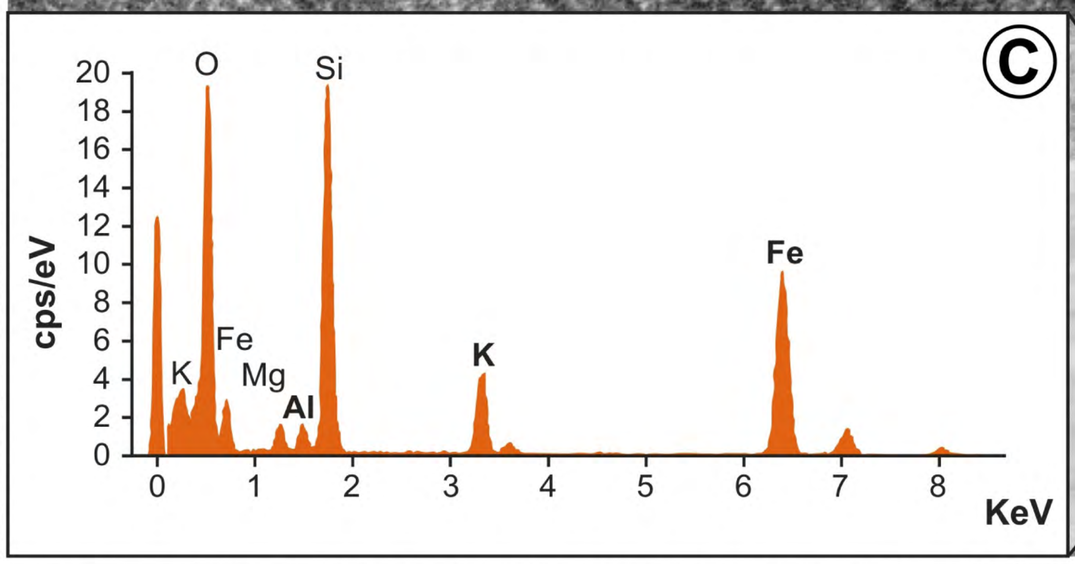
C
cps/eV
O
Si
Fe
K
Mg
Al
K
Fe
KeV

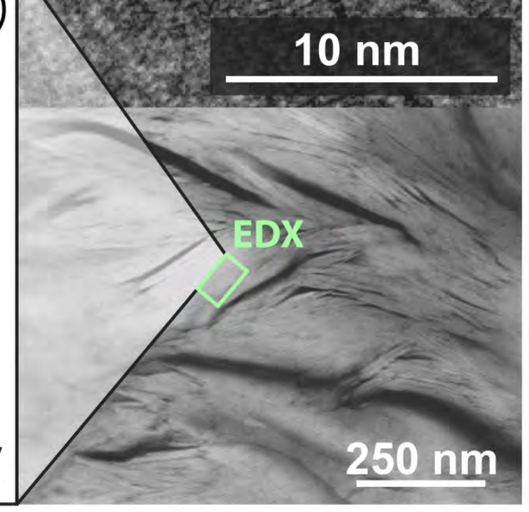
10 nm
EDX
250 nm

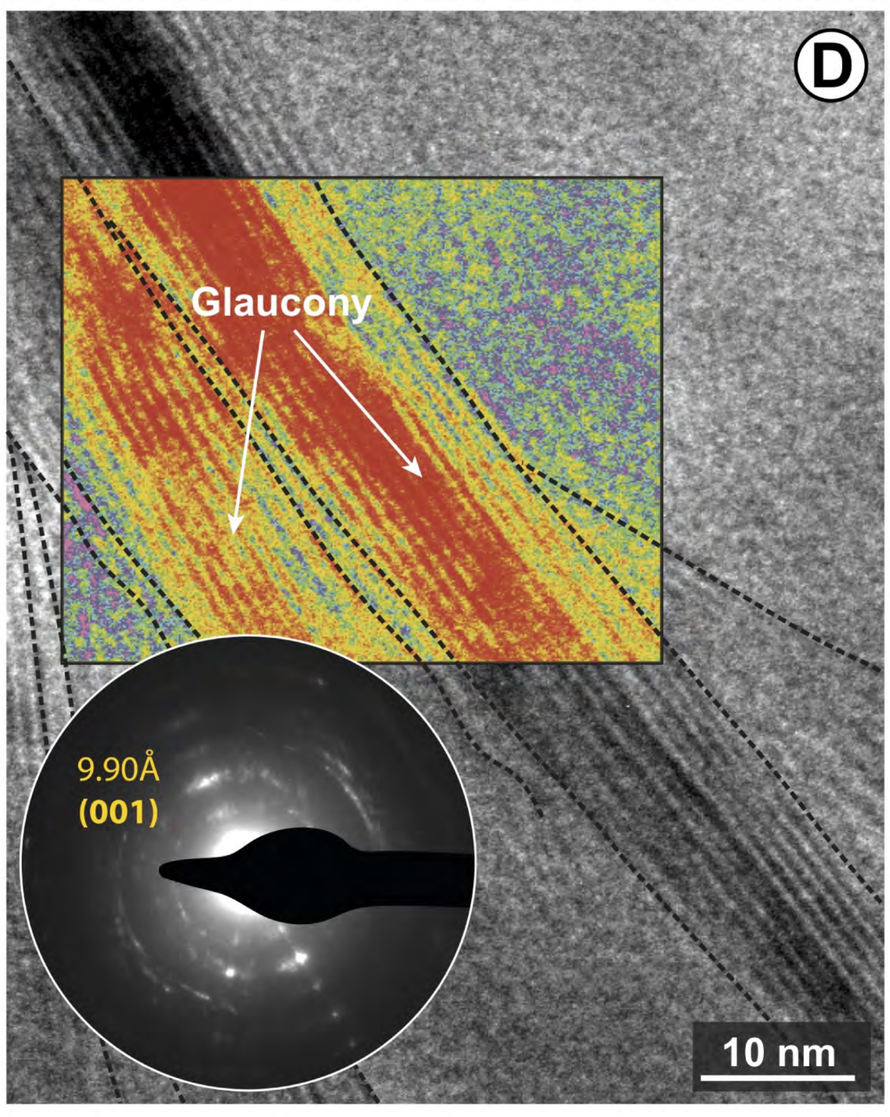
D
Glaucony
9.90Å
(001)
10 nm

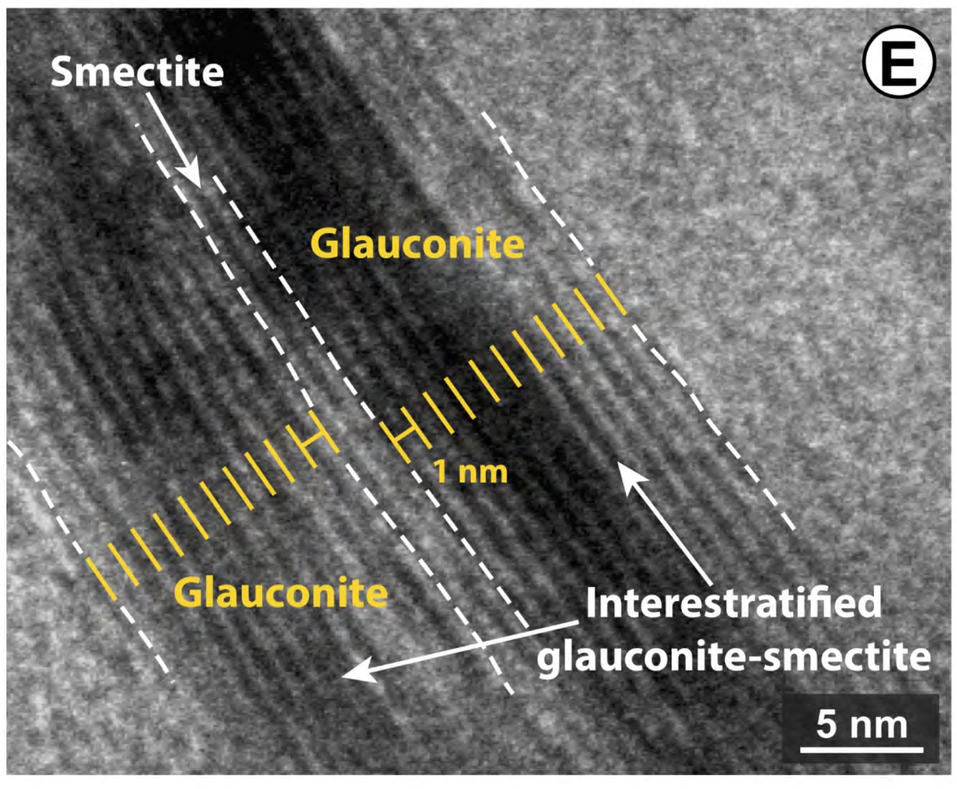
E
Smectite
Glauconite
1 nm
Glauconite
Interestratified
glauconite-smectite
5 nm

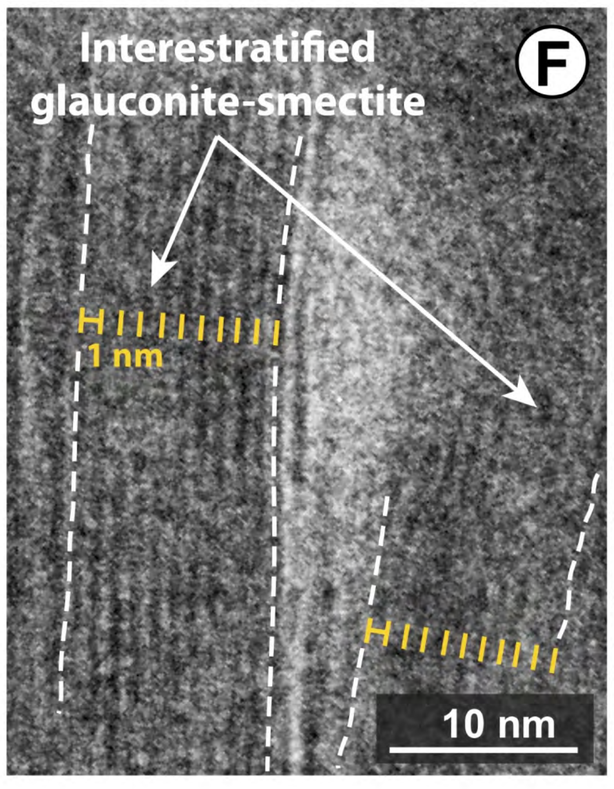
F
Interestratified
glauconite-smectite
1 nm
10 nm

Figure 5

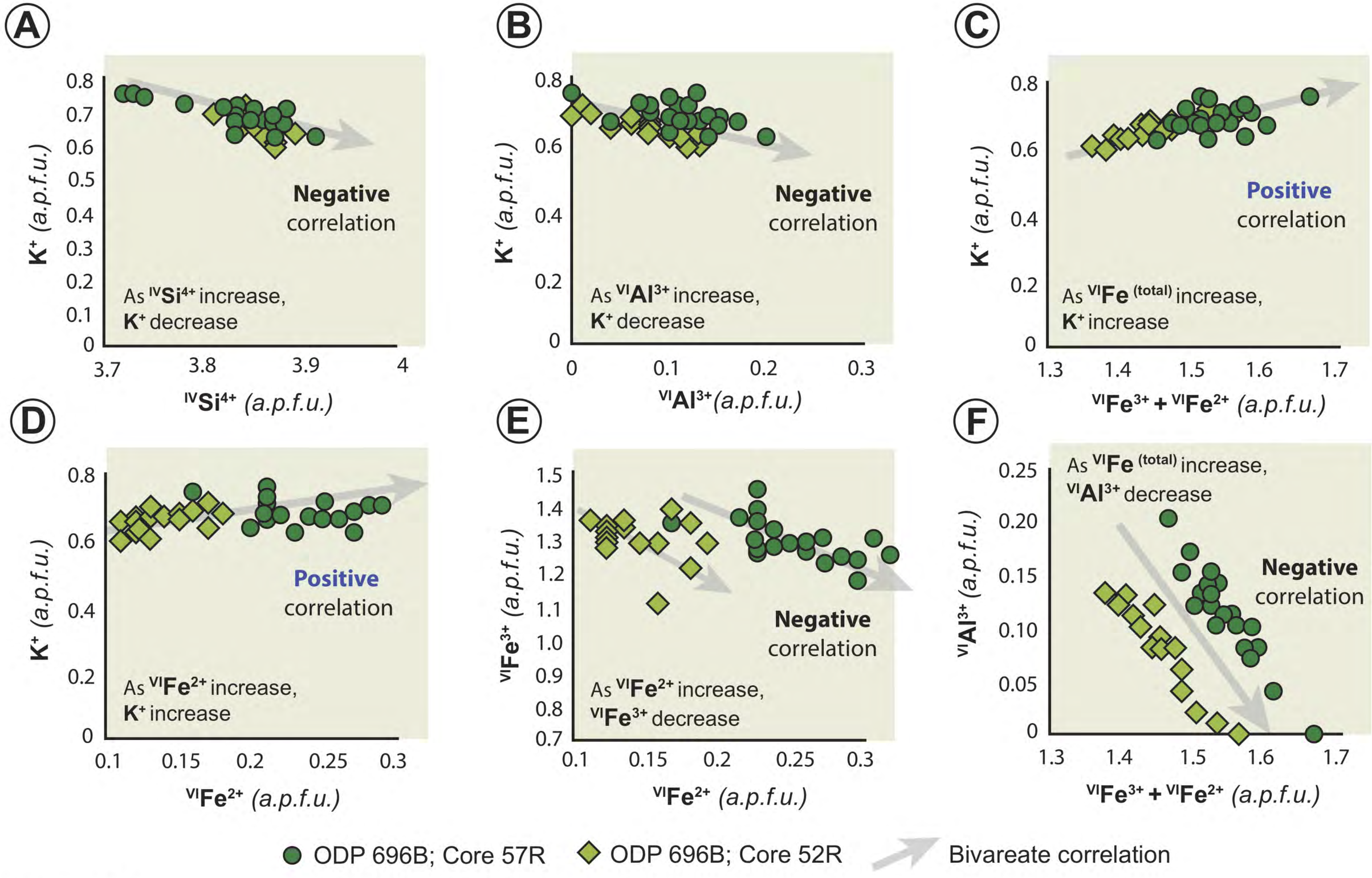
A
B
C
D
E
F
K+ (a.p.f.u.)
IVSi4+ (a.p.f.u.)
Negative correlation
As IVSi4+ increase, K+ decrease
VIAl3+(a.p.f.u.)
As VIAl3+ increase, K+ decrease
VIFe3+ + VIFe2+ (a.p.f.u.)
Positive correlation
As VIFe (total) increase, K+ increase
VIFe2+ (a.p.f.u.)
Positive correlation
As VIFe2+ increase, K+ increase
VIFe3+ (a.p.f.u.)
Negative correlation
As VIFe2+ increase, VIFe3+ decrease
VIAl3+ (a.p.f.u.)
Negative correlation
As VIFe (total) increase, VIAl3+ decrease
ODP 696B; Core 57R
ODP 696B; Core 52R
Bivareate correlation

Figure 6

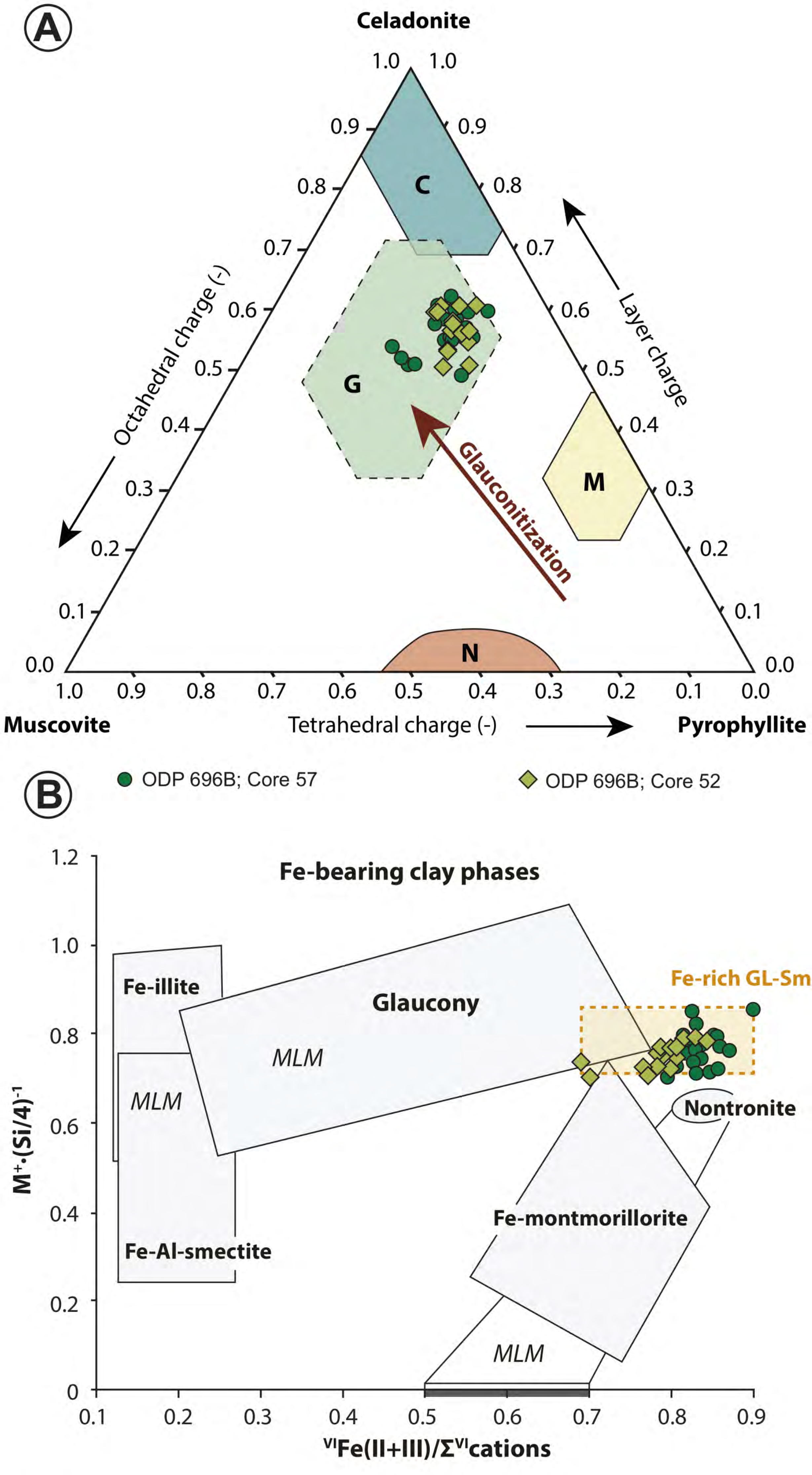
A
Celadonite
1.0
0.9
0.8
0.7
0.6
0.5
0.4
0.3
0.2
0.1
0.0
C
G
M
N
Glauconitization
Octahedral charge (-)
Layer charge
Muscovite
Tetrahedral charge (-)
Pyrophyllite
B
ODP 696B; Core 57
ODP 696B; Core 52
Fe-bearing clay phases
Fe-illite
Glaucony
MLM
MLM
Fe-rich GL-Sm
Nontronite
Fe-montmorillorite
Fe-Al-smectite
MLM
M+·(Si/4)-1
VIFe(II+III)/ΣVIcations

Figure 7

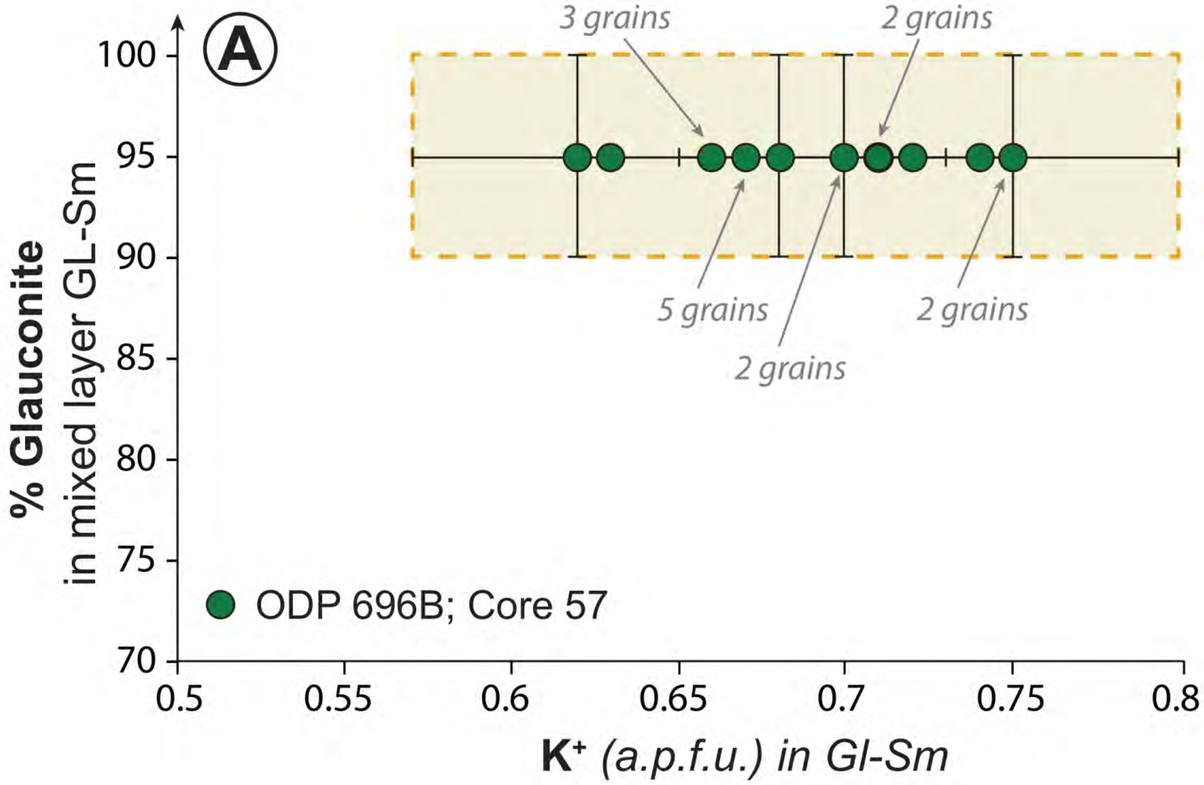
A
3 grains
2 grains
5 grains
2 grains
2 grains
% Glauconite
in mixed layer GL-Sm
ODP 696B; Core 57
K+ (a.p.f.u.) in Gl-Sm

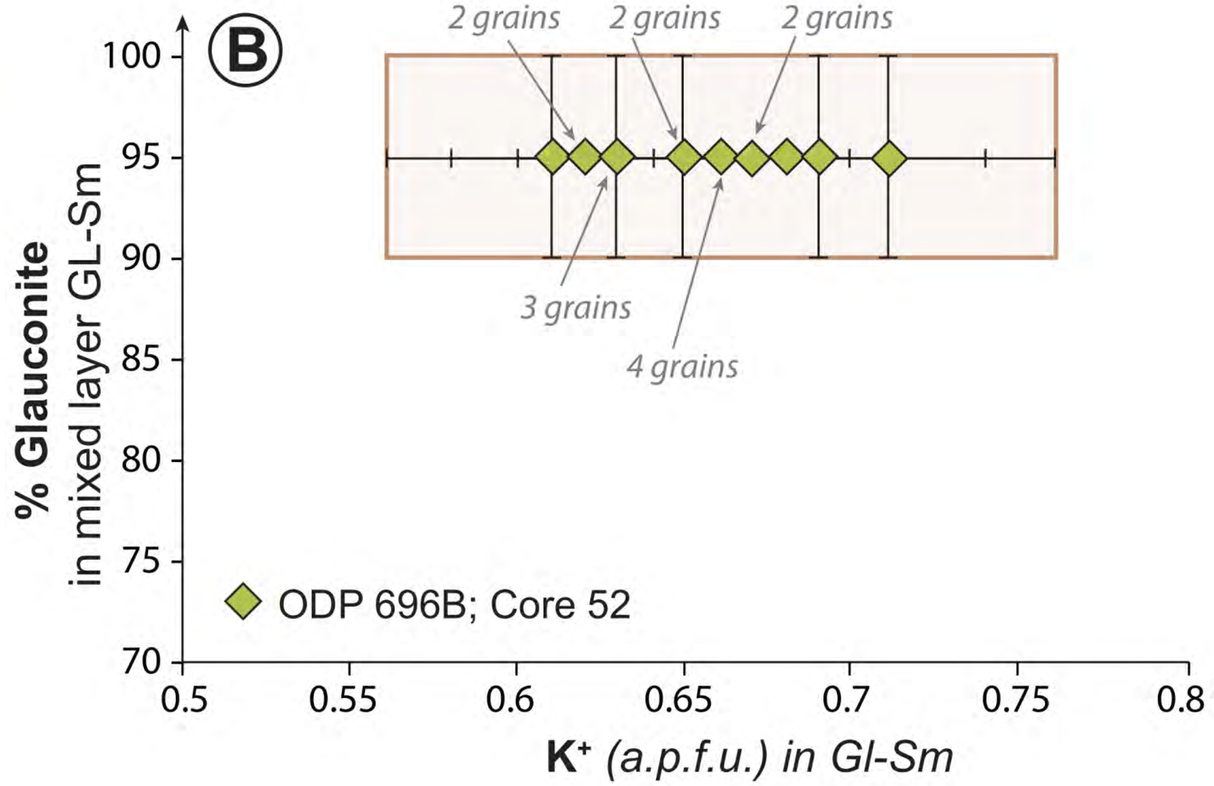
B
2 grains
2 grains
2 grains
3 grains
4 grains
% Glauconite
in mixed layer GL-Sm
ODP 696B; Core 52
K+ (a.p.f.u.) in Gl-Sm

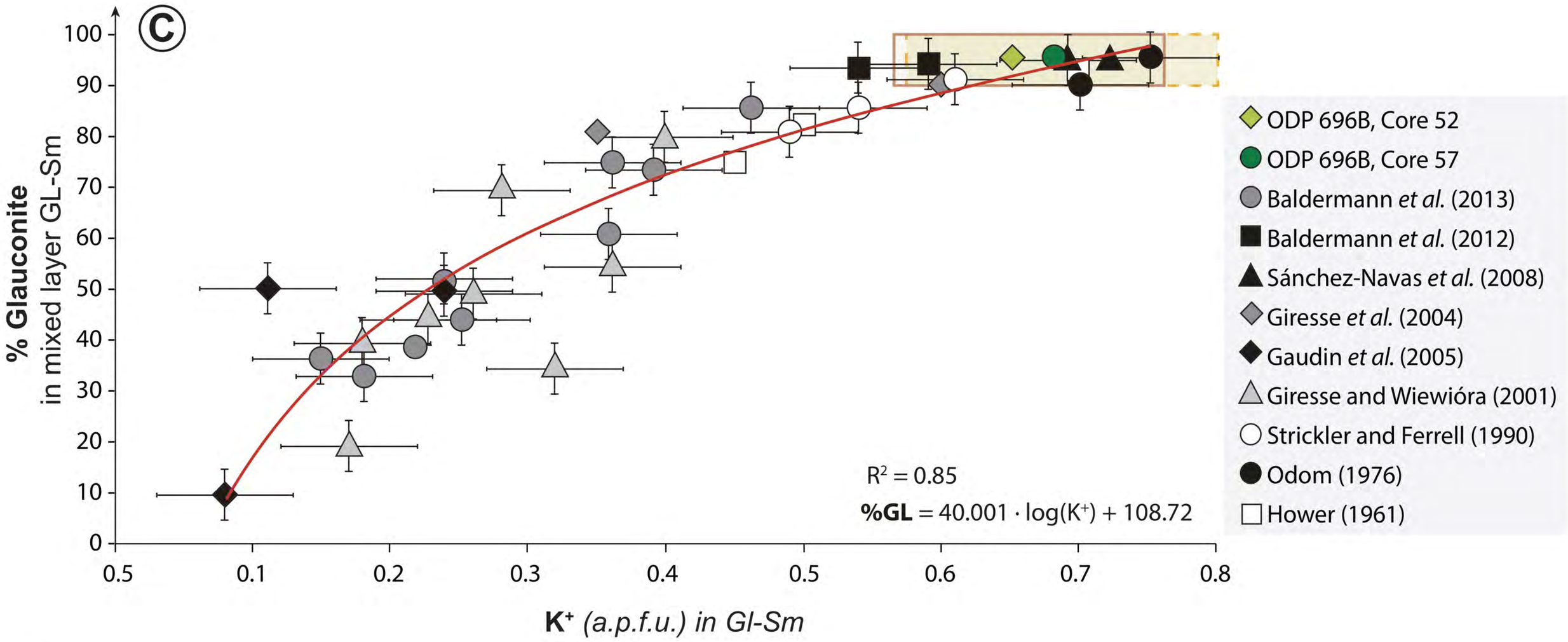
C
% Glauconite
in mixed layer GL-Sm
R² = 0.85
%GL = 40.001 · log(K+) + 108.72
K+ (a.p.f.u.) in Gl-Sm
ODP 696B, Core 52
ODP 696B, Core 57
Baldermann et al. (2013)
Baldermann et al. (2012)
Sánchez-Navas et al. (2008)
Giresse et al. (2004)
Gaudin et al. (2005)
Giresse and Wiewióra (2001)
Strickler and Ferrell (1990)
Odom (1976)
Hower (1961)

Figure 8